HHS Public Access

Author manuscript

Cancer Discov. Author manuscript; available in PMC 2022 February 01.

Published in final edited form as:

Cancer Discov. 2021 August ; 11(8): 1952–1969. doi:10.1158/2159-8290.CD-20-0913.

Intrinsic immunogenicity of small cell lung carcinoma revealed by its cellular plasticity

Navin R. Mahadevan[1,2,+], **Erik H. Knelson**[1,+], **Jacquelyn O. Wolff**[3], **Amir Vajdi**[4], **Maria Saigí**[1], **Marco Campisi**[1,5], **Deli Hong**[1], **Tran C. Thai**[1], **Brandon Piel**[1], **Saemi Han**[1], **Bruce B. Reinhold**[6,7], **Jonathan S. Duke-Cohan**[6,7], **Michael J. Poitras**[8,9], **Luke J. Taus**[8], **Patrick H. Lizotte**[8], **Andrew Portell**[8], **Victor Quadros**[1], **Alison D. Santucci**[1], **Takahiko Murayama**[10], **Israel Cañadas**[10], **Shunsuke Kitajima**[1,11], **Aoi Akitsu**[6,7], **Maya Fridrikh**[12,13], **Hideo Watanabe**[12,13], **Brendan Reardon**[1], **Prafulla C. Gokhale**[8,9], **Cloud P. Paweletz**[8], **Mark M. Awad**[1], **Eliezer M. Van Allen**[1], **Ana Lako**[14], **Xi-Tao Wang**[14], **Benjamin Chen**[14], **Fangxin Hong**[15], **Lynette M. Sholl**[2], **Michael Y. Tolstorukov**[4], **Kathleen Pfaff**[3], **Pasi A. Jänne**[1], **Evisa Gjini**[14], **Robin Edwards**[14], **Scott Rodig**[2,3], **Ellis L. Reinherz**[6,7], **Matthew G. Oser**[1,*], **David A. Barbie**[1,*]

[1]Department of Medical Oncology, Dana-Farber Cancer Institute, Boston, MA 02215 USA

[2]Department of Pathology, Brigham and Women's Hospital, Boston, MA 02115 USA

[3]Center for Immuno-Oncology, Dana-Farber Cancer Institute, Boston, MA 02215 USA

[4]Department of Informatics and Analytics, Dana-Farber Cancer Institute, Boston, MA 02215 USA

[5]Department of Mechanical and Aerospace Engineering, Politecnico di Torino, Turin, 10129, Italy.

[6]Laboratory of Immunobiology, Dana-Farber Cancer Institute, Boston, MA 02215 USA

[7]Department of Medical Oncology, Dana-Farber Cancer Institute and Department of Medicine, Harvard Medical School, Boston, MA 02215 USA

[8]Belfer Center for Applied Cancer Science, Dana-Farber Cancer Institute, Boston, MA 02215 USA

[9]Experimental Therapeutics Core, Dana-Farber Cancer Institute, Boston, MA 02215 USA

[10]Blood Cell Development and Function Program, Fox Chase Cancer Center, Philadelphia, PA 19111 USA

[11]Department of Cell Biology, Cancer Institute, Japanese Foundation for Cancer Research, Tokyo, 135-8550, Japan

[*]**Corresponding authors:** David A. Barbie, 450 Brookline Ave, Boston, MA 02215. david_barbie@dfci.harvard.edu. Phone: 617-632-6036, Matthew G. Oser, 450 Brookline Ave, Boston, MA 02215. moser@partners.org. Phone: 617-582-8668.

[+]These authors contributed equally to this work.

Author Contributions

N.R.M., E.H.K., E.L.R., M.G.O., and D.A.B designed research and wrote the manuscript. N.R.M., E.H.K., M.S., M.C., D.H., S.H., T.T., P.L., A.P., V.Q., T.M., I.C., S.K., A.A. and D.A.B. performed and supervised biological, cellular, and immunologic studies. B.B.R., J.S.D-C, and E.L.R. performed and supervised immunopeptidome studies. N.R.M., E.H.K., J.O.W., M.M.A., L.M.S., X.-T. W., B.C., F.H., E.G., R.E., P.A.J. and S.R. obtained patient samples, performed pathologic review, and performed or supervised immunohistochemistry, oversaw patient sample sequencing, or clinical outcomes analysis. J.W., A.L., K.P., and S.R. performed and supervised multiplexed immunofluorescence. I.C., M.F., and H.W. performed ChIP-Seq and analysis. A.V., M.Y.T., H.W., B.R., and E.A. performed and supervised computational analyses. L.T., M.P., and P.C.G., and C.P. performed and supervised in vivo experiments.

[12]Department of Medicine, Division of Pulmonary, Critical Care and Sleep Medicine, New York, NY 10029 USA

[13]Tisch Cancer Institute, Icahn School of Medicine at Mount Sinai, New York, NY 10029 USA

[14]Translational Pathology, Bristol Myers Squibb, Trenton, NJ 08648

[15]Department of Biostatistics, Harvard T.H. Chan School of Public Health

Abstract

Small cell lung carcinoma (SCLC) is highly mutated, yet durable response to immune checkpoint blockade (ICB) is rare. SCLC also exhibits cellular plasticity, which could influence its immunobiology. Here we discover that a distinct subset of SCLC uniquely upregulates MHC I, enriching for durable ICB benefit. *In vitro* modeling confirms epigenetic recovery of MHC I in SCLC following loss of neuroendocrine differentiation, which tracks with de-repression of STING. Transient EZH2 inhibition expands these non-neuroendocrine cells, which display intrinsic innate immune signaling and basally restored antigen presentation. Consistent with these findings, murine non-neuroendocrine SCLC tumors are rejected in a syngeneic model, with clonal expansion of immunodominant effector CD8 T cells. Therapeutically, EZH2 inhibition followed by STING agonism enhances T cell recognition and rejection of SCLC in mice. Together, these data identify MHC I as a novel biomarker of SCLC immune responsiveness and suggest novel immunotherapeutic approaches to co-opt SCLC's intrinsic immunogenicity.

INTRODUCTION

Small cell lung carcinoma (SCLC) is defined as a high-grade neuroendocrine carcinoma arising in the lung, and virtually all tumors display loss of the tumor suppressor genes, *RB1* and *TP53* (1). While most SCLC patients initially respond to cytotoxic chemotherapy, resistance inevitably emerges, and the 5 year survival rate is dismal (2,3). The addition of immune checkpoint blockade (ICB) to first-line chemotherapy has yielded relatively modest benefit and durable responses are rare, despite SCLC's high tumor mutation burden (4,5).

The pathologic diagnosis of SCLC is classically made by morphology and a limited panel of immunohistochemical stains. Morphological features include small-to-intermediate sized cells with high nuclear-to-cytoplasmic ratio, nuclear molding, and a distinctive nuclear appearance (finely granular chromatin lacking prominent nucleoli), which is associated with the neuroendocrine phenotype. Tumors are overtly malignant, displaying a very high proliferation rate, apoptosis, and necrosis. Neuroendocrine differentiation can be demonstrated by immunohistochemical staining for synaptophysin, chromogranin A, and insulinoma-associated protein 1 (INSM1) (6,7).

While SCLC has been largely approached diagnostically and clinically as a monolithic entity, recent transcriptomic profiling of SCLC cell lines and patient samples has indicated significant inter-tumoral and intra-tumoral heterogeneity. Most broadly, SCLC can be divided into neuroendocrine and non-neuroendocrine subtypes, the former showing classical neuroendocrine morphology, *in vitro* growth in non-adherent tumor clusters, and high expression of the transcriptional regulators, ASCL1 and NEUROD1. Non-neuroendocrine

SCLC comprises approximately 10–15% of all SCLC, tends to show adherent *in vitro* growth with a mesenchymal, non-neuroendocrine morphology (8), downregulates ASCL1 and terminal neuroendocrine markers, such as chromogranin A and synaptophysin, and may upregulate transcription factors such as POU2F3, YAP1, or c-MYC (7,9–12). Additionally, loss of ASCL1 has also been associated with upregulation of AXL (11,13,14). Additionally, non-neuroendocrine SCLC cells have been shown to de-repress specific endogenous retroviruses as well as STING, promoting intrinsic innate immune signaling (13). Furthermore, experiments in genetically-engineered mouse models of SCLC and profiling of human SCLC have also shown the co-existence of neuroendocrine and non-neuroendocrine cells within tumors, and cellular plasticity sufficient to allow conversion between these subtypes (7,12,13,15,16).

The presentation of peptides on MHC I molecules to CD8+ T cells serves as a crucial mechanism of immunosurveillance of the intracellular compartment of all nucleated cells (17). Downregulation of MHC I expression and consequently decreased antigen presentation is a major mechanism of immune escape employed by intracellular pathogens, as well as by malignant cells. In tumor cells, alteration of the MHC I pathway can occur via genetic or epigenetic means, and can affect any component of the MHC I antigen processing and presentation machinery (APM), from the immunoproteasome, to the import and loading of peptides on MHC I in the endoplasmic reticulum via the TAP complex, to export of MHC I-peptide complexes to the plasma membrane (18,19). While tumors of different histologic subtypes have been shown to acquire genetic lesions of MHC I APM, usually as an adaptive response to immune system pressure in the setting of immunotherapy, SCLC has been known to be poorly immunogenic, displaying intrinsically low levels of MHC I (20–22), which has recently been suggested to be the consequence of epigenetic programming (23). However, the intersection of MHC I antigen presentation and SCLC heterogeneity has not been explored.

Here, we profile the cellular and immunologic heterogeneity of SCLC and discover that non-neuroendocrine SCLC derepresses MHC I antigen presentation, which is sufficient to evoke CD8+ T cell-mediated rejection. Patients harboring MHC I high SCLC show long-term durable responses to ICB, thus nominating MHC Class I as a novel biomarker of durable ICB response in this treatment-refractory tumor. Further, we demonstrate that the epigenetic regulator, EZH2, can govern the transition to the non-neuroendocrine phenotype, and that its transient inhibition can prime immunogenicity *in vivo*.

RESULTS

MHC Class I expression is increased in patient SCLC with non-neuroendocrine features and enriches for durable ICB response

Although SCLC lacks effective MHC I antigen presentation (20–22), the spectrum of MHC I expression across SCLC and its relationship to tumor heterogeneity has not been characterized. We therefore profiled a large set of *de novo* primary SCLC patient samples (n = 102, Supplementary Table S1.1) using standard chromogenic immunohistochemistry (IHC) as well as multiplexed immunofluorescence (mIF). The majority (H-score ≤ 30; n = 72, 71%) of SCLC displayed little to no MHC I (MHC $I^{lo/neg}$); however, 15% (H-score

≥140, n = 15) of cases showed uniformly high MHC I expression (MHC I^{hi}) (Fig. 1A; Supplementary Table S1.2). Interestingly, the appearance of MHC I^{hi} tumors varied from that of classic neuroendocrine SCLC, exhibiting a more elongate morphology, variably prominent nucleoli, increased cytoplasm (decreased nuclear:cytoplasmic ratio), and decreased organoid architecture (Fig. 1B, Supplementary Fig. S1A). Careful re-examination of MHC $I^{lo/neg}$ tumors also uncovered multiple cases with focal clusters of tumor cells that expressed high levels of MHC I (MHC I^{foc}) and showed morphology similar to that seen in MHC I^{hi} SCLC (Supplementary Fig. S1A–B).

Bulk RNA sequencing of a small subset of these MHC I^{hi} vs. MHC $I^{lo/neg}$ samples revealed that MHC I^{hi} SCLC upregulated a diverse array of MHC I antigen presentation machinery genes, including *TAP1* and *NLRC5*, and also identified strong enrichment of genes associated with interferon signaling and epithelial-to-mesenchymal transition (EMT) (Fig. 1C, Supplementary Table S1.3). In contrast to other previously identified markers of non-neuroendocrine SCLC such as *POU2F3*, *YAP1*, *MYC*, or *Vascular Endothelial (VE)-cadherin* (7,12,24), the MHC I^{hi} phenotype was more robustly associated with upregulation of the EMT marker AXL (Fig. 1D; Supplementary Fig. S1C; Supplementary Table S1.3), which we previously linked to an innate immune active state in SCLC (13). Using mIF, we confirmed that MHC I^{hi} SCLC tumors exhibited RB loss in all cases (n = 15/15), and showed INSM1 expression in most cases (n = 12/14, 1 case QNS) (Supplementary Fig. 1D; Supplementary Table S1.4), consistent with the given diagnoses of SCLC. Examination of protein expression of ASCL1 and chromogranin (CHGA) showed that MHC I^{hi} SCLC significantly downregulated both markers relative to MHC $I^{lo/neg}$ tumors (Fig. 1E; Supplementary Fig. S1E; Supplementary Table S1.4). Taken together, these findings reveal that, while the MHC I^{hi} state retains some neuroendocrine features, it is significantly associated with downregulation of the key SCLC lineage oncogene, ASCL1, consistent with our morphologic findings that varied from prototypical SCLC.

As an increase in MHC I antigen presentation could impact the immune tumor microenvironment, we spatially characterized immune infiltration in MHC I^{hi} SCLC and MHC $I^{lo/neg}$ SCLC using a multiplexed immunofluorescence assay. MHC I^{hi} SCLC was significantly more infiltrated by CD45+/PD-L1+ immune cells in intratumoral regions, as well as at the tumor/stromal edge, than MHC $I^{lo/neg}$ SCLC. Furthermore, MHC I^{hi} SCLC displayed greater intratumoral infiltration of CD3+ T cells (Fig. 1F; Supplementary Fig. S1F), and CD8α was also identified as one of the top genes enriched in MHC I^{hi} tumors in our RNAseq analysis (rank # 167 out of 16189 genes; Supplementary Table S1.3), indicating enrichment for cytotoxic T cells. While PD-L1 expression was statistically significantly increased in MHC I^{hi} SCLC cells, the absolute expression level was low compared with CD45+/PD-L1+ cells (Fig. 1F; Supplementary Fig. S1F), congruent with previous reports of low PD-L1 expression in SCLC tumor cells (25). Supporting these findings, we also observed similar increases in CD45+/PD-L1+ and CD3+ immune cell infiltration around tumor nests focally expressing high levels of MHC I in MHC I^{foc} tumors, which was not seen in the MHC I low areas of the same tumors (Fig. S1G–H). Taken together, these findings suggest that MHC I^{hi} SCLC is associated with an immune microenvironment primed for an effector response, but one that displays an upregulation of the PD-1/PD-L1 immune checkpoint, primarily on infiltrating immune cells.

Because MHC I antigen presentation is crucial for the adaptive immune effector phase disinhibited by ICB, we hypothesized that patients bearing MHC I^{hi} SCLC may be uniquely responsive to such therapy. We gathered a cohort of SCLC patients treated at the Dana-Farber Cancer Institute enriched for those with exceptional durable responses to ICB (n = 31) (Supplementary Table S1.5–1.6). Strikingly, when stratified by MHC $I^{lo/neg}$ vs MHC I^{hi} expression as defined in our larger cohort, patients with MHC I^{hi} SCLC had dramatically more durable responses to ICB, which translated to a robust increase in overall survival, including when used in the post-first-line setting (Fig. 1G–H; Supplementary Fig. S2A–B). Analysis for potentially confounding variables found that MHC I expression was the only variable that predicted survival after treatment with ICB in our cohort containing exceptional responders (Fig. S2C, Supplementary Table S1.5). We also analyzed a subset of chemorefractory SCLC patients treated with nivolumab +/− ipilimumab on the Checkmate 032 trial (n=18). Although there was only one long term responder, this patient's SCLC also exhibited high MHC I expression, and combined analysis of the DFCI/Checkmate 032 cohorts revealed a significantly higher rate of 12-month durable clinical benefit from ICB in MHC I^{hi} patients compared to MHC $I^{lo/neg}$ patients ($p < 0.001$; Supplementary Fig. S2D). These data demonstrate that, while the majority of human SCLCs are MHC $I^{lo/neg}$, a subset of tumors with non-neuroendocrine/mesenchymal features are MHC I^{hi}, which tracks with durable response to ICB and suggests intrinsic immunogenic capacity of these tumors.

Epigenetic silencing of TAP1 in neuroendocrine SCLC underlies its MHC I antigen presentation defect

The observation of intratumoral heterogeneity in MHC I expression and neuroendocrine phenotype in MHC I^{foc} tumors (Supplementary Fig. S1A–B) suggested cell state plasticity and a possible epigenetic mechanism of regulation. Thus, to explore this further, we used the established *in vitro* human SCLC cell line NCI-H69 (H69) and an isogenic, adherent derivative (referred to hereafter as H69M) that contains an epigenetically distinct non-neuroendocrine subpopulation. These non-neuroendocrine cells are marked by expression of PD-L1 and AXL, and activate interferon signaling similar to patient MHC I^{hi} SCLC (Fig. 2A) (13,26). To systematically identify the loci associated with this epigenetic state change, we performed integrative unbiased global H3K27 ChIPseq and RNAseq analysis. Among the top genes upregulated in H69M enriched for both H3K27Me3 loss and H3K27Ac gain were *TAP1*, *AXL*, and *YAP1* (Fig. 2A; Supplementary Table S2.1). Subset analysis of MHC I APM genes upregulated in H69M using the same method confirmed robust enrichment of mRNA expression and H3K27 acetylation (Ac) peaks in MHC I APM genes in H69M (Supplementary Fig. S3A–B), most notably at the TAP1 locus (Supplementary Fig. S3C). Preferential H3K27Ac gain and reciprocal H3K27Me3 loss at the TAP1 locus was at least as pronounced as the previously validated gene TMEM173 (STING) (Supplementary Fig. S3D–E; Supplementary Table S2.2) (13). Furthermore, we observed significant enrichment of this gene set, especially of TAP1 and AXL, in patient MHC I^{hi} SCLC tumors (Fig. 2B, Supplementary Fig. S3F). These findings confirm concordance between this *in vitro* model and patient samples, and further implicated TAP1 in this differential MHC Class I antigen presentation.

TAP1 forms part of a heterodimer that imports cytosolic peptides into the ER for loading onto MHC I, has been implicated in defective SCLC antigen presentation (20,21), and was highly basally upregulated in bulk H69M cells (Supplementary Fig. S3G). We therefore examined whether recovery of MHC I expression in H69M could be related to this epigenetic de-repression of TAP1. Flow cytometry revealed pronounced recovery of MHC I on H69M cells, specifically within the PD-L1^{hi} subpopulation that marks the non-neuroendocrine/mesenchymal cell state (Fig. 2C) (13). Indeed, further dissection of PD-L1/MHC I^{hi} vs PD-L1/MHC I^{lo} cells confirmed that H69M PD-L1/MHC I^{hi} cells specifically upregulated TAP1 and TMEM173 together with EMT and IFN signatures, while downregulating neuroendocrine gene expression (27) (Fig. 2D–E; Supplementary Table S3.1). Liquid chromatography-data independent analysis mass spectrometry (LC-DIAMS) of MHC I-associated immunopeptidomes of H69, bulk H69M, or purified H69M-PD-L1/MHC I^{hi} cells further demonstrated that H69 cells exhibited a profound defect in presentation of endogenously processed peptides, limited to signal peptides, pathognomonic for TAP1 downregulation (Fig. 2F) (17). Bulk H69M cells exhibited partial rescue of endogenous peptide presentation, while H69M PD-L1/MHC I^{hi} cells showed robust recovery of surface peptide display (Fig. 2G). Indeed, H69M PD-L1/MHC I^{hi} cells exhibited near complete recovery of the diversity of HLA-A2-restricted peptides, in contrast to H69 cells, whose peptide display was restricted solely to signal peptides (Fig. 2H; Supplementary Table S3.2). Thus, transition of SCLC to a non-neuroendocrine/mesenchymal state not only activates innate immune signaling pathways, but directly restores TAP1 expression and consequent antigen presentation, as revealed by direct physical detection of HLA-bound peptides.

We next sought to validate these results in additional SCLC cell lines stratified by adherence in cell culture (8), which tracks with downregulation of neuroendocrine markers and upregulation of AXL (Supplementary Fig. S4A–B) (13). In contrast to neuroendocrine cells, MHC I expression was increased in multiple adherent, non-neuroendocrine SCLC cell lines, and correlated with increased *TAP1* mRNA expression (Fig. 3A). Furthermore, TAP1 over-expression in multiple neuroendocrine SCLC cell lines rescued MHC I expression (Supplementary Fig. S4C–H). Thus, endogenous MHC I antigen presentation is recovered in SCLC in its non-neuroendocrine state and is at least partly related to de-repression of TAP1 epigenetic silencing.

EZH2 inhibition in neuroendocrine SCLC facilitates the conversion to an antigenic non-neuroendocrine phenotype

Our findings of immunogenic plasticity in SCLC associated with response to ICB led us to explore pharmacologic approaches to convert SCLC cell state. Based on our ChIPseq findings and its established role in neuroendocrine cell biology (13,23,28,29), we next evaluated the role of the EZH2 H3K27 methyltransferase in neuroendocrine and non-neuroendocrine SCLC. Global H3K27Me3 levels were decreased in adherent cell lines and inversely related to TAP1 protein expression (Fig. 3B). Furthermore, analysis of SCLC Cancer Cell Line Encyclopedia (CCLE) data revealed anti-correlation between TAP1 and EZH2 expression which tracked with cell line adherence as a surrogate for neuroendocrine status (Fig. 3C, Supplementary Fig. 5A). Short term genetic and/or pharmacologic EZH2

inhibition (Supplementary Fig. S5B–C) in neuroendocrine SCLC slightly increased MHC I expression, and sensitized cells to low dose IFN-γ (0.5 ng/ml) (Supplementary Fig. 5D), consistent with a recent study implicating the polycomb repressor complex 2 (PRC2) complex in MHC I repression (23). Indeed, treatment of multiple neuroendocrine SCLC lines with a variety of PRC2 inhibitors for 6 days revealed that robust recovery of MHC I expression required concomitant type I or type II IFN exposure (Supplementary Fig. S5E–J). However, we also failed to observe AXL induction after this short term EZH2 inhibition, even in H69 cells treated with GSK126 + IFN-γ (Fig 3D), revealing that such exposure might be insufficient to reset this broader epigenetic program.

Given the modest effect of short-term EZH2 inhibition alone on MHC I expression (Supplementary Fig. S5F), we next examined the downstream consequences of treating H69 cells with a 6-day GSK126 pulse and release, to determine whether inhibiting EZH2 could unmask cellular plasticity and intrinsic antigenicity over time. Interestingly, this approach, using multiple EZH2 inhibitors and neuroendocrine SCLC cell lines, facilitated recovery from cell cycle arrest and triggered adherence and expansion of a non-neuroendocrine subpopulation (referred to hereafter as H69EZ-G) that morphologically resembled H69M and upregulated MHC I expression (Supplementary Figs. 6A–D). Similar to patient MHC I^{hi} SCLC and non-neuroendocrine H69M, MHC I^{hi} H69EZ-G cells showed co-expression of AXL (Figs. 3E), highlighting the crucial role of an epigenetic cell state change in the basal upregulation of MHC I antigen presentation in non-neuroendocrine SCLC. Congruently, H69EZ-G cells basally upregulated TAP1 expression and exhibited persistent downregulation of H3K27Me3, specifically within the adherent MHC I^{hi} subpopulation (Fig. 3F; Supplementary Fig. S6E). RNAseq of MHC I^{hi} H69EZ-G cells confirmed a similar phenotype as patient MHC I^{hi} SCLC and MHC I^{hi} H69M cells, with enrichment of IFN signaling, EMT, our previously described SPARCS ERV signature, as well as downregulation of neuroendocrine markers (13) (Fig. 3G, Supplementary Table S4.1). H69EZ-G cells constitutively secreted multiple innate immune cytokines and chemokines comparable to H69M cells (Supplementary Fig. S6F), consistent with intrinsic activation of dsRNA/dsDNA sensors (13). In consonance with their STING de-repression, both H69M and H69EZ-G cells preferentially responded to a cyclic dinucleotide STING agonist with dramatic upregulation of CXCL10, similar to other non-neuroendocrine SCLC models (Fig. 3H). CRISPR-mediated silencing of STING in H69M resulted in a marked downregulation of HLA-ABC expression (Fig. 3I), supporting a key role for nucleic acid sensing in enforcing surface antigen presentation in non-neuroendocrine SCLC. Taken together, these data suggest that EZH2 broadly regulates epigenetic SCLC plasticity, and its inhibition promotes a non-neuroendocrine cell state with intrinsic innate immune signaling, which leads to constitutive MHC I recovery (see schematic in Fig. 3J).

Non-neuroendocrine SCLC is immunogenic *in vitro* and *in vivo*

To determine whether SCLC is intrinsically immunogenic in its non-neuroendocrine state, we utilized a CRISPR-derived Rb1;Trp53;Rbl2/p130 (RPP) SCLC genetically-engineered mouse model (GEMM) generated in a C57BL/6 background (30,31). SCLC lines derived from established tumors gave rise to both neuroendocrine suspension tumor cells (referred to hereafter as RPP cells) and non-neuroendocrine adherent tumor cells (referred to hereafter as

RPP-A cells) with inactivation of the same tumor suppressor genes, where RPP-A cells exhibited a phenotype highly concordant with our RNA-seq data from human cell lines and patient samples (Supplementary Fig. S7A–D; Supplementary Table S4.2). RPP cells were largely devoid of MHC I expression (H2-K^b and H2-D^b) and endogenously processed MHC I-restricted peptide display, which was recovered in RPP-A cells, over independent cell line derivations from independent mice (Fig. 4A; Supplementary Fig. S8A–C). Similar to H69 cells, short-term treatment of RPP cells with an EZH2 inhibitor promoted partial recovery of MHC I in response to a low dose of IFN-γ (Supplementary Fig. S8D).

In support of differential immunogenicity, expression of exogenous ovalbumin (OVA) (32) resulted in basal endogenous presentation of the H2-K^b-restricted ovalbumin antigen, SIINFEKL in RPP-A.OVA cells, but not in RPP.OVA cells (Supplementary Fig. S8E–F), which tracked with killing by cognate OT-I T cells (Fig. 4B). RPP.OVA cells were rendered sensitive by high dose IFN-γ stimulation (Supplementary Fig. S8G), confirming their immunogenic capacity with sufficient extrinsic stimulation.

We next directly interrogated the intrinsic immunogenicity of neuroendocrine or non-neuroendocrine SCLC *in vivo* by subcutaneous inoculation of RPP or RPP-A cells into syngeneic BL6 mice. Strikingly, RPP-A cells formed nascent tumors that were spontaneously rejected over the long term and heavily infiltrated with immune cells, in contrast to RPP cells, which effectively evaded an immune response and formed large tumors over time (Fig. 4C, Supplementary Fig. 9A–B). RPP-A cells generated tumors in immunodeficient NSG mice (Supplementary Fig. 9C), confirming their intrinsic tumorigenic capacity and the requirement for adaptive immunity to mediate their rejection. Furthermore, mixing studies combining RPP-A cells with RPP cells at a 1:4 ratio revealed that RPP-A cells in a mixed population can still recruit T cells *in vitro* and promote rejection in immunocompetent mice (Supplementary Fig. 9D–G), suggesting that immune responses evoked by a minority non-NE population can be sufficient to target neuroendocrine SCLC cells in a heterogenous tumor.

To characterize the immune response against non-neuroendocrine SCLC cells in greater depth, we performed paired single-cell RNA and TCR sequencing of CD45+ immune cells 14 days following RPP or RPP-A tumor cell implantation. Single cell data clustering and gene signature analysis revealed that RPP-A tumors were more heavily infiltrated with CD8+ T cells (Figs. 4D; Supplementary Figs. S10A–C, S11A–D; Supplementary Table S5.1–5.2), whereas RPP tumors were uniquely enriched with multiple immune suppressive M2 macrophage markers (33) (Supplementary Figs. S10A–C, S11E; Supplementary Table S5.1–5.2). Interestingly, TCR clonotype analysis uniquely identified an immunodominant TCR clone (Trav14D-3-DV8, Trbv29) comprising 11% of all TCRs within the RPP-A CD8 T cell population, and two additional expanded clones also expressing Trbv29 (Fig. 4E; Supplementary Table S5.3). Trav14D-3-DV8, Trbv29 TCR clonotypes were not identified in RPP tumors, which did not harbor any expanded T cell clones (Fig. 4E; Supplementary Table S5.4). Moreover, differential gene expression analysis revealed high level granzyme, NKG2 family members (klre1 and klrc1), and Ly6c2 expression (Supplementary Fig. S11F; Supplementary Table S5.3) specific to these Trbv29+ CD8 T cells, suggestive of highly sensitive cytotoxic effectors. Furthermore, while RPP cells exhibited quantitatively greater

numbers of CD4 T cells, only RPP-A tumors showed relative expansion of CD4 T cell clones with transcriptional features of developing effector memory (Supplementary Fig. S11G), consistent with their ability to support a diversity of T cell-mediated immune responses against RPP-A-associated antigens.

We next cloned the immunodominant Trav14D-3-DV8, Trbv29 CD8 TCR into the TCR-null line, BW5147.3 (Supplementary Fig. S12A–B), to assess *in vitro* recognition of RPP versus RPP-A cells. Trav14D-3-DV8, Trbv29 expressing T cells were activated only by RPP-A cells derived from two independent SCLC GEMMs (Fig. 4F; Supplementary Fig. S12C). High-dose IFN-γ stimulation led to an increase in TCR responsiveness to RPP-A cells, but not RPP cells, suggesting unique de-repression of the antigenic determinant of the TCR in RPP-A cells (Fig. 4F). Taken together, these data confirm that non-neuroendocrine SCLC is intrinsically immunogenic and capable of evoking T cell-mediated rejection.

Finally, we sought to determine whether the EZH2-inhibitor induced cell state change in neuroendocrine SCLC could facilitate immune rejection in this syngeneic mouse model. Since EZH2 inhibition can also affect T cells *in vivo* (34), we sought to experimentally isolate our analysis of tumor-intrinsic immunogenicity by examining the effects of EZH2 inhibition on RPP cells *ex vivo* prior to implantation. Similar to our studies in human SCLC cells, pulse treatment with GSK126 followed by subsequent release derived an adherent cell line from the murine RPP cell line. This cell line (RPP-EZ) displayed a morphologic and immunologic phenotype intermediate between RPP and RPP-A, showing adherence but not fully elongate/fibroblastic morphology, with moderate increase in basal MHC I expression and recognition by the immunodominant TCR in the presence of IFN (Fig. 4G; Supplementary Fig. 12D). In consonance with these findings, RPP-EZ tumors displayed significant growth impairment relative to RPP tumors but did not show durable long-term responses (Fig. 4H). Of note, we did not observe *in vitro* proliferation changes or differences in early tumor growth between RPP and RPP-EZ, which, if anything, displayed faster engraftment. Since STING was restored and active in the non-neuroendocrine state, and our *in vitro* data suggested that IFN priming may be necessary to unmask robust immunogenicity, we next tested the effects of the STING agonist, ADU-S100, in our RPP-EZ and RPP syngeneic models. Immune profiling demonstrated a significant increase in immune cell infiltration, including CD4+ and CD8+ T cells, in both RPP and RPP-EZ tumors exposed to STING agonist (Supplementary Fig. S12E). When intratumoral ADU-S100 injection was performed in two independent experiments, long-term durable responses were observed preferentially in RPP-EZ tumors ($p < 0.01$) (Fig. 4H; Supplementary Fig. S12F). Indeed, this combination yielded the most significant improvement in overall survival (Fig. 4I), suggesting that EZH2 inhibition both restores SCLC antigenicity, and can prime therapeutic response to STING agonism.

DISCUSSION

Once considered a uniform diagnosis, SCLC subtyping is rapidly evolving to identify therapeutic vulnerabilities. Here we have uncovered a non-neuroendocrine population of SCLC with intrinsic immunogenicity that enriches for durable response to immune checkpoint blockade. Mechanistic dissection of the epigenetic features that govern this

immunologic plasticity reveal and TAP1 and STING as direct regulators of MHC I antigen presentation, as well as a rationale to combine EZH2 inhibitors with STING agonists in a syngeneic mouse model. In addition to confirming that EZH2 regulates MHC I expression in SCLC (23,35), here, we more broadly demonstrate that transition to a non-neuroendocrine cell state in SCLC leads to robust presentation of MHC I-restricted antigens coupled with intrinsic innate immune signaling, sufficient to cause antigen-specific T cell-mediated rejection in a syngeneic system. Notably, the immunodominant T cell clone we identified recognizes a putative rejection antigen solely presented on non-neuroendocrine cells, suggesting the intriguing possibility that epigenetic modulation may uncover immunopeptidome repertoire plasticity sufficient to reveal immunogenic antigens. Indeed, we previously identified de-repression of unique endogenous retroviruses in this context (13), suggesting the possibility that peptides derived from specific retro-elements, in addition to more canonical mutated neoantigens or tumor associated antigens, could be the source of such immunogenicity. That MHC I^{hi} SCLC displays increased immune infiltration by both CD3+/CD8+ T cells and CD45+/PD-L1+ immune cells suggests that the immune microenvironment of such tumors may be poised for an anti-tumor response but these tumors may avoid elimination via immune checkpoints such as PD-L1, the presence of immunosuppressive leukocyte populations, and/or the concurrent production of immune suppressive cytokines.

Our finding that exceptional durable responders to ICB exhibit this non-neuroendocrine, MHC I^{hi} phenotype and that patients with MHC I^{hi} SCLC more generally show preferential clinical benefit to ICB agrees with recent independent characterization of an inflamed SCLC subtype (36), underscoring the intrinsic immunogenicity of this SCLC population and suggesting that immune cell PD-L1 expression may be an important immunosuppressive mediator in this context. Furthermore, a biomarker to stratify ICB responders from non-responders in SCLC is sorely needed. While the incorporation of ICB has improved response rates to first-line treatment in SCLC, overall survival remains limited and new biomarkers could help select patients who are expected to progress in order to facilitate enrollment in clinical trials. In contrast to non-small cell lung cancer (NSCLC), tumor cell PD-L1 levels in SCLC are uniformly low and fail to predict ICB response (37,38). While tumor mutation burden (TMB) tracks to some degree with clinical benefit to ICB in SCLC (39), these cancers possess a high number of mutations overall given their close association with cigarette smoking. Furthermore, TMB is a continuous rather than discrete variable, and it lacks precision to explain differential antigenicity. In contrast, tumor cell MHC I is the ultimate target of CD8 T cells that are re-invigorated by ICB, and hence it is not surprising that MHC I status separates out the patients with SCLC who are able to achieve durable response. While larger cohorts of patients will be necessary to validate these results, MHC I, as well as other features of this non-neuroendocrine state, could serve as straightforward and much-needed biomarkers for ICB response in SCLC.

By integrating epigenetic and expression profiling, and protein expression across our HLA+ cell line models and patient SCLC, we provide an initial description of the MHC I^{hi} SCLC phenotype relative to the current paradigm in the literature. Broadly, we find that MHC I^{hi} SCLC does not express the neuroendocrine markers, ASCL1 or NEUROD1, nor other more recently proposed markers of a non-neuroendocrine state, such c-MYC or YAP1. Instead,

MHC I^{hi} SCLC is enriched for expression of AXL, a state marker for EMT, which appears--like MHC I APM--to be regulated epigenetically. Corroborating our findings, a recently described inflamed SCLC subtype also demonstrates a similar non-neuroendocrine transcriptional signature marked by expression of AXL and upregulation of immune genes, including those involved with MHC Class I APM (36). Additionally, this finding has strong parallels to the melanoma literature where the MITF lineage specific oncogene is also downregulated in an AXL positive innate immune active state (40). These data thus not only identify AXL upregulation as an important feature of the non-neuroendocrine state, but also a novel paradigm for innate immune regulation that has parallels across lineage-oncogene driven tumors.

Since the MHC I^{hi} phenotype results in unique responsiveness to STING agonists, including upregulation of the T cell chemoattractant CXCL10, these populations may especially evoke T cell infiltration upon STING pathway stimulation (41,42). Indeed, we provide initial evidence in a murine model that *ex vivo* EZH2 inhibition can convert neuroendocrine SCLC to an antigenic cell state that is responsive to STING agonism *in vivo*. Future preclinical therapeutic studies could focus on combining EZH2 inhibitors (or other epigenetic inhibitors that alter the SCLC cell state) with STING agonists to overcome the intrinsic immunotherapy resistance of the SCLC neuroendocrine state (43). This will require pharmacodynamic/pharmacokinetic optimization of clinical grade EZH2 inhibitors and STING agonists that are currently in development. While work remains to elucidate the cellular and immunologic interplay of neuroendocrine and non-neuroendocrine SCLC subpopulations, identification of non-neuroendocrine subpopulations in human SCLC via cell state or immunologic profiling may also prove useful in stratifying patients for additional types of immunotherapy including cancer vaccines. Indeed, as these subpopulations are likely to have escaped immune editing (44) they are likely to possess an immunopeptidome enriched for (neo)antigens, resulting in particular vulnerability to immune attack.

METHODS

Patient samples

102 cases of FFPE (formalin fixed paraffin embedded) primary resections of SCLC were obtained from various commercial tissue vendors (BioChain Institute Inc. Newark, CA; Discovery Life Science, Huntsville, AL; Indivumed GmbH, Lewisburg, PA; The MT Group Inc. Van Nuys, CA). All cases had been reviewed by board-certified pathologist at CRO (New England Pathology Associates, PC, Springfield, MA) on H&E slides to ensure tumor content. FFPE sections at 4 μm were prepared and stored at 4°C until use. All cases were deemed histologically compatible with SCLC after expert pathologic review (N.R.M., L.M.S.). SCLC diagnosis in MHC I$^{hi/foc}$ cases was supported with tumor cell-specific RB-inactivation in all cases.

For clinical correlation studies, DFCI/BWH SCLC patients from 2014 – 2019 were selected who had received ICB (n = 31) via electronic medical record (EMR) review. This cohort was enriched for patients with exceptional responses (stable disease/partial response for greater than 1 year). MHC I IHC was performed as below, and scoring used the same cutoffs as

detailed in the text and below. Clinical course information, including radiography and pathology, was abstracted from the EMR and pathology information systems (Powerpath). Targeted next generation sequencing data was abstracted from institutional targeted NGS (Oncopanel) (45) results. All patients provided written informed consented for this research under DFCI protocol 02–180. SCLC human tumor samples were collected and analyzed according to Dana–Farber/Harvard Cancer Center institutional review board-approved protocols. These studies were conducted according to the Declaration of Helsinki and approved by Dana–Farber and Brigham and Women's Hospital institutional review boards. An additional cohort of n=18 FFPE samples was obtained from the Checkmate 032 trial of nivolumab +/− ipilimumab in recurrent SCLC (30). Demographic information was used to ensure no overlap with the DFCI/BWH cohort. After MHC I IHC as described below, survival and response analyses were performed.

Immunohistochemical studies and multiplexed immunofluorescence

Staining of MHC Class I (HLA-A, HLA-B, and HLA-C, 1:6000 dilution, clone EMR8–5, Abcam, Cambridge, UK, Cat. No. ab70328) for all cases (n = 102) and chromogranin (1:5000 dilution, clone LK2H10, Thermo Fisher, Waltham, MA, Cat. No. MS-324-PABX), as well as AXL (1:4000 dilution, clone EPR19880, Abcam, Cambridge, UK, Cat. No. ab219651) for the MHC $I^{hi/foc}$ (n = 17) cases and a randomly selected subset of MHC $I^{lo/neg}$ (n = 40) cases, was performed with a BOND RX fully automated stainer (Leica Biosystems). Formalin-fixed, paraffin embedded tissue sections were baked for 2–3 hours at 40°C then loaded into the BOND RX. Slides were deparaffinized (BOND DeWax Solution, Leica Biosystems, Wetzlar, Germany) and rehydrated through a series of washes of graded ethanol to deionized water. Antigen retrieval (BOND Epitope Retrieval Solution 1 or 2, Leica Biosystems) was performed at pH 6.0 (chromogranin) or 9.0 (MHC class I and AXL) for 30 minutes at 98°C. Slides were then stained with primary antibodies for 40 minutes. Next, rabbit anti-mouse IgG (Post Primary, BOND Polymer Refine Detection Kit, Leica Biosystems) was applied for 10 minutes, then subsequently detected by anti-rabbit Polymeric Horseradish Peroxidase (Poly-HRP, BOND Polymer Refine Detection Kit, Leica Biosystems). Finally, slides were counterstained with hematoxylin, dehydrated in graded alcohol and xylene, and mounted with EcoMount mounting medium (Biocare Medical, Concord, MA). Pathologists S.J.R. and N.R.M. assigned an H-score (range, 0 to 300) to each sample by multiplying the percentage of tumor cells positive for MHC class I staining (0% to 100%) by the average intensity of staining (0 to 3+) of the tumor cells. The cutoff for MHC I^{hi} cases was calculated to include extreme outliers of a positively skewed distribution: median + 2.5 interquartile ranges. The same method of assigning an H-score was used by pathologist N.R.M to score chromogranin and AXL staining.

Multiplexed immunofluorescence staining was performed with the BOND RX fully automated stainer (Leica Biosystems). Formalin-fixed, paraffin embedded tissue sections were baked for 3 hours at 60°C then loaded into the BOND RX. Slides were deparaffinized (BOND DeWax Solution, Leica Biosystems) and rehydrated through a series of washes of graded ethanol to deionized water. Antigen retrieval (BOND Epitope Retrieval Solution 1, Leica Biosystems) was performed at pH 6.0 for 30 (RB) or 10 (all other target antigens) minutes at 98°C. Slides were then stained with primary antibodies with an incubation time

of 40 minutes. As an additional step for mouse antibodies, rabbit anti-mouse IgG (Post Primary, BOND Polymer Refine Detection Kit, Leica Biosystems) was applied for 10 minutes. The slides were then incubated with anti-rabbit Polymeric Horseradish Peroxidase (Poly-HRP, BOND Polymer Refine Detection Kit, Leica Biosystems) for 10 minutes. Next, the slides were incubated with Opal Fluorophore Reagents (Akoya Biosciences, Marlborough, MA) for 5 minutes to visualize signal of the antibody complexes. This process was repeated for all antibodies included in a panel. The target antigens, antibody clones, and dilutions for Panels 1 and 2 are listed in Supplementary Table S6.1. Slides were then manually counterstained with DAPI (NucBlue Fixed Cell ReadyProbes Reagent, Invitrogen, Carlsbad, CA), washed with deionized water, air dried, and mounted with ProLong Diamond Anti-fade Mountant (Invitrogen).

A minimum of four representative images per sample were obtained using the Mantra Quantitative Pathology Workstation (Akoya Biosciences) at 20 × magnification. Following image acquisition, each field of view was spectrally unmixed and analyzed using inForm 2.4 Image Analysis Software (Akoya Biosciences). Images were manually categorized into tumor and stromal regions using inForm's tissue classification tool. All nucleated cells within a field of view were then identified via nuclear DAPI (4′,6-diamidino-2-phenylindole) staining. Using a supervised machine-learning algorithm within the program, each cell was assigned a phenotype according to biomarker expression within its defined nuclear and membrane compartments. For cases of sufficient image quality stained with Panel 1, an H-score for ASCL1 and INSM1 was generated by setting intensity thresholds for 0–3 binning (from 0 for "no signal" to 3 for "strong signal") under pathologist supervision. The percent of cells in each intensity bin was multiplied by the value of that bin (i.e, 0–3), and the combined scores automatically produced an H-score in the inForm software. For each case, an average H-score was calculated based on 4–10 representative fields of view. Cells phenotypically determined to be non-malignant were excluded from analysis. To quantify immune infiltrate in cases stained with Panel 2, a minimum threshold of positive staining was assigned for each image, categorizing cells as negative or positive for a particular biomarker. To calculate cell density of a biomarker (per megapixel), the percent of positive cells was multiplied by the total number of cells present in the tissue category, divided by the number of pixels in the tissue category, then divided again by the conversion factor of 1,000,000 (pixels per megapixel). For each case, an average H-score was calculated based on 5–12 representative fields of view. When quantifying biomarker expression in malignant cells, cells phenotypically determined to be non-malignant were excluded from analysis.

Cell lines

Use of human SCLC cell lines NCI-H69, H69M (parental, control, and STING KO) NCI-H82, NCI-H2081, and NCI-H196 was continued from our prior work[6]. The human SCLC cell line, CORL47, was kind provided by Dr. M. Oser. The murine lymphoma cell line, BW5147.3 was obtained from the laboratory of E. Reinherz. COLO668 and 293T cells were obtained from the American Type Culture Collection (ATCC, Rockville, MD).

H69, H69M, H69EZ-G, H82, H2081, and CORL47 were cultured in RPMI-1640 (Thermo Fisher Scientific, #11875–119) containing 10% FBS (Cat# 100–106, Gemini Bio-products, West Sacramento, CA), 1X penicillin/streptomycin (Cat# 15140122, Thermo Fisher Scientific, Waltham, MA), and prophylactic Plasmocin (2.5 mg/mL; Cat# ant-mpp, Invivogen, San Diego, CA). H196 and 293T were maintained in Dulbecco's Modified Eagles Medium (DMEM) (Cat# 11965–118, Thermo Fisher Scientific) containing 10% FBS and 1X penicillin/streptomycin. RPP and RPP-A cell lines were cultured in RPMI (Cat# 11875–119, Thermo Fisher Scientific), containing 10% FBS (Cat# 100–106, Gemini Bio-products), 1X penicillin/streptomycin (Cat# 400–109, Gemini Bio-Products, Sacramento, CA), and HITES [1X insulin-transferrin-selenium (Cat# I3146, Sigma-Aldrich, St. Louis, MO), 10 nM β-estradiol (Cat# E2257, Sigma-Aldrich), and 10 nM hydrocortisone (Cat# 10687010, Thermo Fisher Scientific)]. BW5147.3 was maintained in DMEM (Cat# 11965–118) containing 10% FBS, 1X penicillin/streptomycin (Cat# 15070063), 400 μg/mL G418 (Cat# 10131035) (Thermo Fisher Scientific), and 400 μg/mL hygromycin (Cat# H0135, Sigma-Aldrich). All cell lines were routinely monitored for mycoplasma using the Takara PCR Mycoplasma Detection Set (Cat# 6601, Kusatsu, Shiga, Japan), and were negative.

Quantitative RT-PCR

Total cellular RNA was extracted using the RNeasy Mini Kit (Qiagen, Hilden, Germany) according to manufacturer's instructions. After extraction, 500 ng-1 μg total RNA was used to generate cDNA with the SuperScript III First-Strand Synthesis SuperMix for qRT-PCR kit, which includes both oligo-dT and random primers (Thermo Fisher Scientific, Waltham, MA). Quantitative reverse transcription PCR (qRT-PCR) of the indicated genes was performed using SYBR green PCR Master Mix (Applied Biosystems, Foster City, CA) and the Applied Biosystems 7300 Fast real-time PCR system and software. Target gene expression was normalized to *36B4*, and analyzed using the –ΔΔCt relative quantification (RQ) method. The sequences of primers used have been listed in Supplementary Table S6.2.

Immunoblotting and ELISA

Protein was isolated from cell lines and measured by BCA (Pierce Biotechnology, Rockford, IL). Protein extracts were subjected to polyacrylamide gel electrophoresis using the 4%–12% NuPAGE gel system (Invitrogen, Carlsbad, CA), transferred to PVDF (Millipore) membranes, and immunoblotted using antibodies (Cell Signaling Technologies, Danvers, MA) that specifically recognize TAP1 (Cat# 12341), EZH2 (clone D2C9, Cat# 5246S), H3K27Me3 (clone C36B11, Cat# 9733), STING (clone D2P2F, Cat# 13647S) and β-Actin (Cat# 4970). Secondary antibodies were from LICOR Biosciences (Lincoln, NE): IRDye 800CW Goat 495 anti-Mouse IgG (H + L) (Cat# 926–32210), and IRDye 800CW Goat anti-Rabbit IgG (H + L) (Cat# 926–22 32211). LICOR blocking buffer (Cat# 927–40000) was used to dilute primary and secondary antibodies, with the exception of the anti-TAP1 antibody, which was diluted in HIKARI Signal Enhancer Solution 1 (Cat# NU00101, Nacalai USA, Inc. Kyoto, Japan). Imaging of blots and quantitation of bands was performed using the LICOR Odyssey system.

Proteome Profiler™ Human Cytokine Array Kit (Cat# ARY005B), human and mouse CXCL10 ELISA (Cat# SIP100, and DY466), and mouse IL-2 ELISA (Cat# M2000) were

performed according to manufacturer's (R&D Systems, Minneapolis, MN) instructions. For cytokine array, conditioned media (CM) from SCLC cells at basal conditions was collected after 48 hours. For CXCL10 ELISA, CM was collected after 24 h. For IL-2 ELISA, CM from SCLC-T cell cocultures was collected after 72 hours.

Flow cytometry analysis

Single mouse tumor cell suspensions were generated using the mouse Tumor Disassociation Kit (Cat# 130–096-730, Miltenyi Biotec, Bergisch Gladbach, Germany) per manufacturer's protocol using the gentleMACS Octo Disassociator with heaters using the 37C_m_TDK1 protocol. After RBC lysis and filtration, cell suspensions were subjected to flow cytometry. For extracellular staining, after live/dead staining with Zombie NIR Fixable Viability Kit (Cat# 423106, Biolegend, San Diego, CA) per manufacturer's instructions, single cell suspensions were stained with fluorophore-conjugated primary antibodies (see Supplementary Table S6.3), in PBS containing 2% FBS at 2 μg/mL. For experiments with intracellular staining, after live/dead and extracellular staining, cells were fixed in fresh 4% paraformaldehyde and permeabilized in 100% ice-cold methanol for 30 minutes. After washing, cells were incubated with fluorophore conjugated anti-H3K27Me3 (Cat# 12158, clone C36B11, Cell Signaling Technologies, Danvers, MA) at 1:100 dilution. After washing, cells were resuspended in PBS containing 2% FBS and analyzed on a LSRFortessa flow cytometer (Becton Dickinson, Franklin Lakes, NJ). Levels were compared with isotype control antibodies. Cell cycle analysis was performed using the BD Cycletest Plus kit (Cat# 340242, BD Biosciences, San Jose, CA) per manufacturer's protocol. The data analyses were performed with FlowJo software (TreeStar).

HLA immunoprecipitation and LC-DIAMS

Pan-HLA immunoprecipitation was performed as previously described (46). Briefly, adherent cells were released non-enzymatically to preserve surface antigen expression by incubation at 37°C for 30 min in non-enzymatic cell dissociation medium (PBS supplemented with EDTA [5 mM], EGTA [5 mM] and FCS [1%]). Following centrifugation, the cell pellet ($0.5 – 1 \times 10^6$ cells) lysed (Triton X-100, 1.2%; octyl-β-D-glucopyranoside, 1.77%; Tris-HCl, 20 mM; EDTA, 1 mM; NaCl, 100 mM; complete protease inhibitor cocktail, ×1; Roche, Basel, Switzerland) and incubated on ice 20 min. Lysed cells were centrifuged for 10 min at 21,000 g and the supernatant was centrifuged for 1 h at 105,000 g (Airfuge; Beckman-Coulter, Brea, CA) and 4°C to pellet cellular debris. The lysate was then added to the anti-monomorphic HLA Class I antibody (clone W6/32; Biolegend, San Diego, CA) pre-incubated Protein G Sepharose beads (GE Healthcare, Chicago, IL) and rotated for 3 h at 4°C. The lysate-bead suspension was then centrifuged at 900 g for 3 min and the supernatants retained for confirmation of depletion of HLA Class I. The beads were then washed ×6 in wash buffer (0.5 mL/wash; octyl-β-D-glucopyranoside, 1.77%; Tris-HCl, 20 mM; EDTA, 1 mM; NaCl; 100 mM) followed by ×2 washes in salt buffer (Tris-HCl, 20 mM; EDTA, 1 mM; NaCl; 100 mM). Residual liquid was removed using fine pipette tips and the bead samples with bound HLA-peptide stored at −80°C until processed for MS analysis.

All Poisson detection MS methodology and liquid chromatography (LC) data independent acquisition (DIA) MS methodologies were performed as described previously(46). In brief, mass spectra were collected on a quadrupole-TOF (Sciex 6600+, Framingham, MA) instrument in a DIA format. The m/z region 400–680 was split into 11 minimally overlapping windows of variable width designed to transmit equal ion fluxes with MHC-class I immune peptidomes. MS data were collected in a series of a single full-range MS spectrum followed with 11 MS/MS spectra for each transmitted window. The MS/MS spectra were compared with reference patterns obtained from synthetic peptides using an algorithm based on the theory of sampling a Poisson process. High LC-MS sensitivity was promoted using electrospray ionization with 20μm ID alkane modified polystyrene-divinylbenzene monolithic columns (fabricated in-house) at flow rates of roughly 10 nl/min. Elution positions of the synthetic peptides relative to shared endogenous immune peptides using the same column configuration were also determined, and this provides a restrictive map for the elution positions of the epitope candidates in the tumor DIA MS data.

Bulk RNAseq for cell line and patient SCLC samples

For cell line comparison, RNA was isolated directly from duplicate or triplicate samples with the Qiagen (Hilden, Germany) RNeasy isolation kit (Cat# 8028) using on-column DNAse digestion. RNA libraries were prepared from 250 ng total RNA using the Illumina Exome Capture kit per manufacturer's instructions. RNA-sequencing (RNA-seq) was performed per the standard protocols at the Dana-Farber Molecular Biology Core Facilities with Illumina NextSeq 500 instrument. Data quality controls and replicate correlation were evaluated using VIPER software package (47).

For patient samples, thirty (30) blocks, comprised of all MHC I^{hi} cases (n=15) and MHC $I^{lo/neg}$ cases (n=15), were submitted for paired whole genome and transcriptome sequencing. Samples with less than 70% overall tumor content were scribed by a pathologist to enrich for tumor. Up to 10 consecutive FFPE 5μM sections were macrodissected or whole slide scraped and pooled into a single tube for downstream DNA and RNA isolation. DNA and RNA were co-extracted using the Qiagen AllPrep kit (Qiagen Cat No./ID: 80204). DNA and RNA were qualified and quantified using Nanodrop and Qbit to determine concentration and Agilent Bioanalyzer to determine quality. RNA samples with less than 100ng were excluded from downstream analysis. RNA sequencing libraries were prepared using the TruSeq Illumina Stranded Total Gold with RiboZero using 100 ng of total RNA. Libraries were quantified and qualified using KAPA library quantification kits (Cat No. 07960255001) and Bioanalyzer and all samples with a less than 2nM library concentration were excluded from sequencing. Libraries were sequenced on the Novaseq to a read depth of 80 million paired-end reads with 100 bases read lengths. These data are deposited in the GEO database under accession GSE168295.

Differential gene expression analysis for both cell line and patient sample bulk RNA-seq data was performed using the R package, DESeq2 (48). Gene Set Enrichment Analysis (GSEA) of bulk RNA-seq data was performed using the generated lists of differentially expressed genes with R package ClusterProfiler (49) for the Hallmark Gene Sets from MSigDB collection (50), Neuroendocrine marker genes (27), and SPARCS gene signature

set (13). The GSEA P-values were adjusted with the al Benjamini-Hochberg method and the adjusted P-value threshold was set to 0.05. Visualization of the results and downstream analyses were performed using R software (r-project.org).

H3K27 ChIP-seq

ChIP-seq was performed as described previously (51). Briefly, cells were crosslinked with 1% formaldehyde for 10 min, washed in 5 mg/ml bovine serum albumin (BSA) before re-suspended in lysis buffer (50 mM Tris-HCl pH 8.1, 10 mM EDTA, 1% SDS, 1× protease inhibitor cocktail) and sonicated with the Covaris M220 sonicator to obtain chromatin fragment lengths of 100-to-1,000 bp. Fragmented chromatin was diluted in IP buffer (20 mM Tris-HCl pH 8.1, 150 mM NaCl, 2 mM EDTA, 1% Triton X-100) and incubated with Protein G magnetic beads (Dynabeads, Thermo Fisher Scientific, Waltham, MA) pre-incubated with anti-H3K27Ac (ab4729, Abcam, Cambridge, UK) or anti-H3K27me3 (clone C36B1, Cell Signaling Technologies, Danvers, MA) antibodies. Immunoprecipitates were washed six times with wash buffer (50 mM HEPES pH 7.6, 0.5 M LiCl, 1 mM EDTA, 0.7% Na deoxycholate, 1% IGEPAL CA-630) and twice with TE buffer. Immunoprecipitated (or no IP input) DNA was treated with RNase A and Proteinase K on the beads, and recovered in 1% SDS and 0.1 M NaHCO3. Up to 10 ng of DNA was used for the library construction using NEBNext Ultra II DNA Library Prep Kit (Cat# E7645, New England Biolabs, Ipswich, MA). Sequencing was performed on NextSeq500 (Illumina, San Diego, CA) for 38 nucleotides each from paired ends according to the manufacturer's instructions.

Sequenced reads were aligned to human reference genome hg19 by bowtie2 with default settings with -k 1 parameter. After removing duplicate reads with samtools, ChIP-enriched regions (peaks) were identified by MACS (52). ChIP signals for each sample was visualized on integrative genome viewer (IGV) genome browser (53) using wiggle files with a 10 bp resolution for H3K27ac modification and 1kb resolution for H3K27me3 modification generated by MACS with tag shift that was rescaled to normalize to a total number of uniquely alignable sequences by WigMath function of Java-Genomic Toolkit. These data are deposited in the GEO database under accession GSE168195.

The H69M upregulated genes (1,326) were used to identify associated H3K27ac peaks found in H69M or H69 cells, resulting in 4,937 peaks. H3K27me3 signal and H3K27ac signal normalized by MAnorm algorithm were used to draw scatter plot for deltas and log fold changes, respectively and plotted. The thresholds of 3.0 logFC for H3K27ac and −3 delta for H3K27me3 were used to identify 78 epigenetically differential genes which were further filtered with differentially expressed genes in H69M vs H69 at the threshold of −4.0 DEseq2 score described above to identify 72 epigenetically regulated genes. Similarly, to determine whether MHC class I antigen presenting machinery was enriched, 823 genes from reactome ID R-HSA-983169 (Class I MHC mediated antigen processing & presentation) was used to run ssGSEA analysis against rank ordered DEGs between H69M vs. H69. The 91 genes overlapping between 1,326 H69M upregulated genes and 823 Class I MHC antigen presentation and processing genes were used to identify associated H3K27ac peaks found in H69M or H69 cells, resulting in 319 peaks. H3K27me3 signal and H3K27ac signal normalized by MAnorm algorithm were used to draw scatter plot for deltas and log fold

changes, respectively. Heatmap was drawn using H3K27me3 signal and H3K27ac signal around the 319 peaks and clustered by hierarchical clustering using deepTools.

TAP1 over-expression

The full-length human TAP1 sequence was obtained from the Harvard PlasmID database and cloned into the pLX_304 vector using the Gateway system (Thermo Fisher Scientific, Waltham, MA). A pLX_304 vector bearing nanoLuc (nLuc) was used as a control. NCI-H82 and CORL47 cells were transfected by nucleofection (AmaxaTM 4D-Nucleofector X Unit) according to the manufacturer's instructions (Lonza, Basel Switzerland), and maintained under blasticidin (10 μg/mL) selection.

CRISPR-Cas9 gene editing and lentiviral infection

Oligonucleotides coding for guide RNAs that target the EZH2 gene was chosen from the Avana library and the Brunello library (54). A non-targeting sgRNA from the Gecko library v2 was used as a control (ctrl) sgRNA (55). LentiGuide vectors were cloned as previously described (55,56). sgRNA target sequences are listed in Supplementary Table S6.4. 293T cells were transduced using X-treme Gene 9 (Roche, Basel, Switzerland) according to the manufacturer's instructions. 72h supernatant of transduced 293T cells was collected through a 0.45 μm filter and added to the target NCI-H82.Cas9 cells (gift from M. Oser) in the presence of polybrene (8 μg/mL). Cells and virus were centrifuged for 30 minutes at 2000 rpm at 37^{O} C for 2 h. On day 5, puromycin and blasticidin was added to select infected cells.

Compounds and treatments

Recombinant human IFN-γ (Cat# 285-IF) and IFN-β (Cat# 8499-IF), and murine IFN-γ (Cat# 485-MI) and IFN-β (Cat# 8234-MB-010) cytokines were purchased from R&D Systems (Minneapolis, MN) and reconstituted in 1% BSA. For STING agonism experiments, cells were treated with ADU-S100 (50 μM, Cat# CT-ADUS100, ChemieTek, Indianapolis, IN) for 24 h. For EZH2 inhibition experiments, cells were treated with the indicated concentrations of EZH2 inhibitor (GSK126, Cat# 15415, Cayman Chemical Company, Ann Arbor, MI; CPI-1205, Selleck Chemicals, Cat# S8353, Houston, TX; EPZ-6438 was obtained from the laboratory of Jun Qi) or DMSO for 6 days. EZH2 inhibitor was replenished on day 3 with all cells carried each time. After the EZH2 inhibitor treatment period, equal numbers of control or drug-treated cells were exposed to the indicated concentrations of IFN-γ or IFN-β for 24 hours before harvesting of RNA or flow cytometry. For H69EZ-G and RPP-EZ derivation, GSK126 (5 μM)-treated or control cells were thoroughly washed twice in PBS and all cells recultured in cell culture medium without drug. Cultures were routinely passaged as necessary and were examined daily for the emergence of adherent populations.

Cytokine profiling

Multiplex assays were performed utilizing the bead-based immunoassay approach Bio-Plex Pro™ Human Cytokine 40-plex Assay (Cat# 171AK99MR2) on a Bio-plex 200 system (Cat# 171000201) (Bio-Rad Laboratories, Hercules, CA) and the Human Cytokine/ Chemokine Magnetic Bead Panel (Cat# HCYTMAG-60K-PX30) on a Luminex MAGPIX

system (Merck Millipore, Billerica, MA). Conditioned media concentration levels (pg/mL) of each protein were derived from 5- parameter curve fitting models. Fold changes relative to the corresponding control were calculated and plotted as log2FC. Lower and upper limits of quantitation (LLOQ/ULOQ) were imputed from standard curves for cytokines above or below detection.

Ovalbumin-luciferase transduction and OT-I CTL assay

RPP and RPP-A cell lines were transduced to stably express OVA antigen using the pLVX-lucOS-IRES-Neo lentiviral vector (32). CD8+ T cells were isolated from 8–12 weeks old C57BL/6-Tg (TcraTcrb)1100Mjb/J OT-I mice (stock #003831; Jackson Laboratory) using magnetic separation and LS columns per manufacturer's protocol (Cat# 130–049-401; Miltenyi Biotec, Bergisch Gladbach, Germany). OT-I T cells were activated with Dynabeads Mouse T-Activator CD3/CD28 beads (Cat# 11456D, Thermo Fisher Scientific, Waltham, MA) for 24 hours before co-culture. RPP.OVA and RPP-A.OVA cells (target) were seeded in 96 well plates at a density of 10,000 cells per well and co-cultured with activated OT-I CD8+ T cells (effector) at effector to target (E:T) ratios of 0, 1, 5, and 10 for 48 hours. Tumor cell survival was measured by luminescence as previously described (32). Percent survival was calculated by dividing luminescence of each E:T ratio by luminescence of appropriate tumor cell condition without T cells, and percent specific tumor cell lysis was calculated as 100 – percent survival.

Murine SCLC GEMM, cell line derivation, and tumor implantation studies

The RPP SCLC mouse cell lines were derived from SCLC tumors that were generated in LSL-Cas9 BL6 mice that were intratracheally injected with AAV that encode Cre-recombinase and sgRNAs targeting Rb1, Trp53, and Rbl2 (RPP) (30,31). Once tumors developed, independently-infected mice (631 and 703) were euthanized with CO2 and their tumors were quickly extracted, washed in ice cold PBS, and minced several times using an ethanol sterilized razor blade. 3 mL of collagenase/hyaluronidase (Cat# 07912, Stemcell Technologies, Vancouver, CA) diluted 1:10 in RPMI media containing 10% FBS, penicillin and streptomycin, and HITES, and 1 mL dispase (Cat# 354235, Corning, Corning, NY) was added to the tumor, and incubated at 37° C for 20–40 minutes (until most of the tumor cells were in suspension). The cells were then collected, centrifuged at 201 × g for 5 minutes, resuspended in RPMI HITES media, filtered through a 70 μm cell strainer (Cat# 352350, Becton-Dickinson, Franklin Lakes, NJ), centrifuged again at 1000 rpm for 5 minutes, resuspended in fresh RPMI HITES media and placed in ultra-low adherence tissue culture dishes (Cat# 3471, Corning). Media was subsequently replaced every 3 days. Histopathology of the tumor from which the cell lines were derived showed small cell lung cancer. Immunoblot analysis was used to confirm expression of the neuroendocrine transcription factor ASCL1 and Cas9. RPP-adherent (RPP-A) derivatives of the parental cell line was established by plating cells on tissue culture plates at 200,000 cells/mL for 4 days and the supernatant containing suspension cells and replacing with fresh complete media every 3–4 days until the RPP-A cell lines were established. CRISPR amplicon sequencing of the 631RPP and 631RPP-A cell lines was performed as described previously (30). Unless otherwise indicated, RPP and RPP-A designations refer to tumor cells derived from the 631 mouse (631RPP and 631RPP-A (30)).

8×10^6 RPP, RPP-A, or RPP-EZ cells in 1:1 PBS:Matrigel (Corning #354234) were subcutaneously (s.c.) injected into the flank of 8 week old syngeneic C57/BL6 or NSG mice (Charles River Laboratories, Wilmington, MA) anesthetized with isoflurane. Tumor volume was determined from caliper measurements of tumor length (L) and width (W) according to the formula $(L \times W)^2/2$. Both tumor size and body weight were measured three times per week. RPP-EZ tumors were injected with vehicle or ADU-S100 treatments (first treatment, 50 μg; second treatment, 35 μg) on day 19/23 for larger cohort (n=7) and on day 21/24 for smaller cohort (n=3 mice per group). Mice were euthanized at pre-set or humane endpoints and tumors collected and processed with gentleMACS C tubes (Miltenyi 130–093-237) per manufacturer's protocol prior to flow cytometry. All experiments were conducted in accordance with a Dana Farber Cancer Institute Institutional Animal Care and Use (IACUC) approved protocol.

Single cell (sc)-RNA and TCR sequencing

Viable CD45+ (20000) and CD3+ (30000) cells were isolated via FACS from pooled RPP or RPP-A tumors, washed, assessed for viability, and loaded onto a 10X Chromium instrument (10X Genomics, Pleasanton, CA) per the manufacturer's instructions. Single-cell RNA and TCR libraries were generated using the Chromium Single Cell 5' Library Construction (Cat# PN-1000020) and Chromium Single Cell V(D)J Enrichment Kit, Mouse T Cell kits (Cat# PN-1000071) (10X Genomics) per user guide. Quality control of the completed libraries was performed using the Bioanalyzer High Sensitivity DNA Kit (Cat# 5067–4626, Agilent, Santa Clara, CA) and then sequenced using the Illumina NextSeq 500 platform.

Single cell RNA-seq data were aligned to the mouse genome (mm10). After initial filtering with default parameters, the feature matrix generated by Cell Ranger v 3.0.2 was used to perform downstream analysis using R toolkit Seurat (v.3.1.3) (57). Cells expressing less than 100 or more than 7,000 genes, and cells with more than 20% of UMIs mapping to mitochondrial genes were removed from consideration. Additionally, genes that were expressed in less than 6 cells were filtered out. The filtered matrix was log-normalized with scaling factor 10000, centered gene-wise and then underwent dimensionality reduction using principal component analysis (PCA) on the highly varying genes. Clustering was performed on the chosen principal components using the shared nearest neighbor algorithm as implemented in Seurat, with top 50 dimensions. The clusters were visualized using UMAP algorithm. Marker genes for each cluster were identified with Seurat's function FindMarkers (Wilcoxon Rank Sum test without thresholds). To identify dominant cell type in each cluster we used the enrichment analysis using AUCell R package(58), using cell type-specific previously published signatures (59). TCR chain assembly was performed using the Cell Ranger pipeline, with default parameters. Cells with low confidence or non-productive TCR were filtered out. Cells with at least one alpha or beta chain were used in integrative analysis with the transcriptome data. A clonotype was assigned to a specific cell type (cluster) if majority of the cells with this clonotype belonged to the corresponding cluster. To integrate RPP and RPP-A data sets, functions FindIntegrationAnchors and IntegrateData were applied using top 20 dimensions of the transcriptome data. Approaches similar to those describe above were used to perform clustering and identify cell types in the integrated data set, and

function AverageExpression was used to obtain average expression of the genes within a cell type for RPP and RPP-A populations.

TCR cloning, lentiviral infection, and T cell coculture

TCR cloning into *Tcra;Tcrb*-null BW5147.3 cells was adapted from Holst et al. (60) and as described in Brazin et al. (61). Briefly, the *Trbv29-Trbc1-P2A-Trav14D-3-DV8-Trac1* minigene derived from TCR sequencing data was commercially synthesized (Integrated DNA Technologies, Newark, NJ) using optimized constant regions, and Gateway *attb1* and *attb2* sites were added via PCR cloning. The minigene was cloned into the Lenti plx_307 backbone and 293T cells were transduced using X-treme Gene 9 (Roche, Basel, Switzerland) according to the manufacturer's instructions. On day 2 the supernatant of transduced 293T cells was collected through a 0.45 μm filter and added to the target cells in the presence of polybrene (8 μg/mL). Cells and virus were centrifuged at 2000 rpm at 37^{O} C for 2 h. On day 5, puromycin (1 μg/mL) was added to select infected cells. After expansion, selected cells were sorted to >98% purity using an anti-mouse pan-TCR-β antibody (Cat# 109211, clone H57–597, Biolegend, San Diego, CA) expression (BD FACSMelody).

Tumor cell-T cell cocultures were performed at a stimulator: responder (S:R) ratio of 1:1. 100000 tumor cells were seeded in a 24 well plate and stimulated or not with IFN-γ (100 ng/mL) for 24 h. Tumor cells were washed once in PBS, and replated in cell culture medium. After washing, 100000 parental BW5147.3 or transgenic Trav14D-3-DV8, Trbv29 transgenic T cells were added to tumor cells and co-cultures were incubated for 72 h, after which cell-free supernatant was harvested for ELISA.

3D Migration Assay

Mouse cell-derived tumor spheroids were generated from RPP and RPP-A cells by seeding 1 × 10^6 cells into a 6-well ultra-low attachment (ULA) dish (Corning, Cat.# 3471) and incubating at 37 C°, 5% CO2 for 24 hours. Spheroids were stained with Cell Tracker Red (Thermo Fisher Scientific, Cat.# C34552) to allow identification using fluorescence microscope. Collagen hydrogel was formulated to a concentration of 2.5 mg/mL using type I rat tail collagen (Corning, Cat. #354236) following the addition of 10 × PBS with phenol red with pH adjusted using NaOH to 7.0 to 7.5 range, which was confirmed using PANPEHA Whatman paper (Sigma-Aldrich) as previously described (62,63). The spheroids were then pelleted and resuspended in 250 μL of collagen hydrogel, and 10 μL of collagen-spheroid suspension was pipetted into the central gel region of each device of the microfluidic chip (AIM Biotech, Cat.# DAX-1) to generate a 3-D tumor microenvironment model. The devices were incubated for 40 minutes at 37°C in humidity chambers to allow ample collagen polymerization. After polymerization, fluorescently stained T cells (eBioscience cell proliferation dye eFluor 450, #65–0842), were resuspended in RPMI supplemented with 10% FBS, 1% penicillin–streptomycin, and 2 -mercaptoethanol. 200 μL of T cell suspension, containing 5×10^{4} cells, was loaded into the fluidic channel one side of the device. 200 μL RPMI supplemented media without cells was added to the media channel of the other side of the microfluidic device.

After 72 to 96 hours of incubation (37C, 5% CO2), T cell migration was measured. Whole devices were imaged using a Nikon Eclipse 80i fluorescence microscope equipped with Z-stack-capable stage (Prior) and an Andor Zyla camera (Andor). Image capture and analysis was performed using the NIS-Elements AR software package. Whole device images were created by stitching in multiple captures at 4x magnification with 5% overlap. 9 z-stacks were taken 10 μm apart. Using the NIS software, an Extended Depth of Focus (EDF) image was generated, merging the multiple z-stacks into a single image. A binary layer was added to the image to exclude pixels below background intensity. A rectangular region of interest (ROI) was drawn encompassing the gel area, and the binary area (μmˆ2) within the ROI was measured using the software's measurement tool. Quantification of cell migration/infiltration into the 3-D tumor microenvironment was performed by measuring the total cell area of cell tracker dye in the entire gel region as binary area.

Statistical analyses

All graphs depict mean ± s.e.m unless otherwise indicated. Tests for differences between two groups were performed using two-tailed unpaired Student's t-test or two-tailed Mann-Whitney test as specified in the figure legends. One-way ANOVA and Bonferroni correction was performed where applicable. Log-rank test was utilized for patient and mouse survival analyses. Chi Square test was used to compare observed and expected proportions with MHC^{hi} in our clinical cohort of patients experiencing durable clinical benefit from ICB (defined as 12-month progression free survival). P values were considered significant if less than 0.05. Asterisks used to indicate significance correspond with: *p<0.05, **p<0.01, ***p<0.001, ****p<0.0001. GraphPad Prism 9 was used for statistical analysis of experiments, data processing and presentation.

Supplementary Material

Refer to Web version on PubMed Central for supplementary material.

Acknowledgements

The authors thank Jun Qi for reagents, as well as Marina Vivero and Maurizio Zanetti for insightful discussions on this work. Additionally, we thank the BMS Translational Pathology Histology Core Laboratory for preparation of H&E and unstained slides, and the Dana-Farber/Harvard Cancer Center in Boston, MA, for the use of the Specialized Histopathology Core, which provided histology and immunohistochemistry service. This work was supported by NIH R01CA190294 (DAB), the Parker Institute for Cancer Immunotherapy (DAB, ELR), Dunkin Donuts Award (DAB, ELR), Schaubert Family Funds (DAB), Gross-Loh Research Fellowship (EHK), and BMS II-ON Funding (DAB, SR). Additional funding was provided by NIH T32HL7627–35 and NIH T32CA251062 (NRM), NCI-T32 CA009172 (EHK) and NCI/NIH K08CA222657 (MGO), Damon Runyon Cancer Research Foundation Clinical Investigator Award (MGO), Kaplan Family Funds (MGO), MIT-POLITO grant BIOMODE, Compagnia di San Paolo, under the joint "Doctorate of Bioengineering and Medical-Surgical Sciences" of University of Turin and Politecnico di Torino (MC), and Fundación CRIS contra el cáncer Grant (MS).

Dana-Farber/Harvard Cancer Center is supported in part by an NCI Cancer Center Support Grant # NIH 5 P30 CA06516. Further, we would like to thank the Sequencing Facility of the Department of Oncological Sciences at Icahn School of Medicine at Mount Sinai (ISMMS) for sequencing assistance. This work was supported in part through Tisch Cancer Institute at ISMMS and the computational resources and staff expertise provided by Scientific Computing at ISMMS. Research reported in this paper was supported by the Office of Research Infrastructure of the National Institutes of Health under award numbers S10OD018522 and S10OD026880. The content is solely the responsibility of the authors and does not necessarily represent the official views of the National Institutes of Health.

We thank Anika Adeni, Kesi Michael, and Arrien Bertram for assistance in obtaining patient specimens. We are grateful to Benjamin Ferland, Thomas Thayer, and Teri Bowman for technical assistance and Jennifer Largaespada and Hannah Cassatly for superior administrative assistance. We are grateful to Neal Lindeman, Lecia Sequist, Jim DeCaprio, Camille Kotton, Anna Farago, and Jacob Sands for invaluable mentoring throughout this project.

Conflicts of Interest

D.A.B. is a consultant for Qiagen/N-of-One and Tango Therapeutics, has received research support from Bristol Myers Squibb, Novartis, Lilly, Gilead Sciences, and is a founder and shareholder in Xsphera Biosciences. M.G.O. has Sponsored Research Agreements with Lilly Pharmaceuticals and Takeda Pharmaceuticals. A.L., X.-T.W., B.C., E.G., and R.E. are employees of Bristol Myers Squibb. E.H.K. has a Sponsored Research Agreement with Takeda Pharmaceuticals. P.A.J. has received consulting fees from AstraZeneca, Boehringer-Ingelheim, Pfizer, Roche/Genentech, Takeda Oncology, ACEA Biosciences, Eli Lilly and Company, Araxes Pharma, Ignyta, Mirati Therapeutics, Novartis, LOXO Oncology, Daiichi Sankyo, Sanofi Oncology, Voronoi, SFJ Pharmaceuticals, Takeda Oncology, Transcenta, Silicon Therapeutics, Bayer, Esai and Biocartis; receives post-marketing royalties from DFCI owned intellectual property on EGFR mutations licensed to Lab Corp; has sponsored research agreements with AstraZeneca, Daichi-Sankyo, PUMA, Boehringer Ingelheim, Eli Lilly and Company, Revolution Medicines and Astellas Pharmaceuticals; and has stock ownership in LOXO Oncology and Gatekeeper Pharmaceuticals.

REFERENCES

1. George J, Lim JS, Jang SJ, Cun Y, Ozretic L, Kong G, et al. Comprehensive genomic profiles of small cell lung cancer. Nature 2015;524(7563):47–53 doi 10.1038/nature14664. [PubMed: 26168399]
2. Gazdar AF, Bunn PA, Minna JD. Small-cell lung cancer: what we know, what we need to know and the path forward. Nat Rev Cancer 2017;17(12):765 doi 10.1038/nrc.2017.106.
3. Wang S, Tang J, Sun T, Zheng X, Li J, Sun H, et al. Survival changes in patients with small cell lung cancer and disparities between different sexes, socioeconomic statuses and ages. Sci Rep 2017;7(1):1339 doi 10.1038/s41598-017-01571-0. [PubMed: 28465554]
4. Horn L, Mansfield AS, Szczesna A, Havel L, Krzakowski M, Hochmair MJ, et al. First-Line Atezolizumab plus Chemotherapy in Extensive-Stage Small-Cell Lung Cancer. N Engl J Med 2018;379(23):2220–9 doi 10.1056/NEJMoa1809064. [PubMed: 30280641]
5. Yarchoan M, Hopkins A, Jaffee EM. Tumor Mutational Burden and Response Rate to PD-1 Inhibition. N Engl J Med 2017;377(25):2500–1 doi 10.1056/NEJMc1713444. [PubMed: 29262275]
6. Travis WD, Brambilla E, Nicholson AG, Yatabe Y, Austin JHM, Beasley MB, et al. The 2015 World Health Organization Classification of Lung Tumors: Impact of Genetic, Clinical and Radiologic Advances Since the 2004 Classification. J Thorac Oncol 2015;10(9):1243–60 doi 10.1097/JTO.0000000000000630. [PubMed: 26291008]
7. Rudin CM, Poirier JT, Byers LA, Dive C, Dowlati A, George J, et al. Molecular subtypes of small cell lung cancer: a synthesis of human and mouse model data. Nat Rev Cancer 2019;19(5):289–97 doi 10.1038/s41568-019-0133-9. [PubMed: 30926931]
8. Gazdar AF, Carney DN, Nau MM, Minna JD. Characterization of variant subclasses of cell lines derived from small cell lung cancer having distinctive biochemical, morphological, and growth properties. Cancer Res 1985;45(6):2924–30. [PubMed: 2985258]
9. Borromeo MD, Savage TK, Kollipara RK, He M, Augustyn A, Osborne JK, et al. ASCL1 and NEUROD1 Reveal Heterogeneity in Pulmonary Neuroendocrine Tumors and Regulate Distinct Genetic Programs. Cell Rep 2016;16(5):1259–72 doi 10.1016/j.celrep.2016.06.081. [PubMed: 27452466]
10. Simpson KL, Stoney R, Frese KK, Simms N, Rowe W, Pearce SP, et al. A biobank of small cell lung cancer CDX models elucidates inter- and intratumoral phenotypic heterogeneity. Nature Cancer 2020;1(4):437–51 doi 10.1038/s43018-020-0046-2.
11. Pearsall SM, Humphrey S, Revill M, Morgan D, Frese KK, Galvin M, et al. The Rare YAP1 Subtype of SCLC Revisited in a Biobank of 39 Circulating Tumor Cell Patient Derived Explant Models: A Brief Report. J Thorac Oncol 2020;15(12):1836–43 doi 10.1016/j.jtho.2020.07.008. [PubMed: 32721553]

12. Ireland AS, Micinski AM, Kastner DW, Guo B, Wait SJ, Spainhower KB, et al. MYC Drives Temporal Evolution of Small Cell Lung Cancer Subtypes by Reprogramming Neuroendocrine Fate. Cancer Cell 2020;38(1):60–78 e12 doi 10.1016/j.ccell.2020.05.001. [PubMed: 32473656]
13. Canadas I, Thummalapalli R, Kim JW, Kitajima S, Jenkins RW, Christensen CL, et al. Tumor innate immunity primed by specific interferon-stimulated endogenous retroviruses. Nat Med 2018;24(8):1143–50 doi 10.1038/s41591-018-0116-5. [PubMed: 30038220]
14. Muller J, Krijgsman O, Tsoi J, Robert L, Hugo W, Song C, et al. Low MITF/AXL ratio predicts early resistance to multiple targeted drugs in melanoma. Nat Commun 2014;5:5712 doi 10.1038/ncomms6712. [PubMed: 25502142]
15. Calbo J, van Montfort E, Proost N, van Drunen E, Beverloo HB, Meuwissen R, et al. A functional role for tumor cell heterogeneity in a mouse model of small cell lung cancer. Cancer Cell 2011;19(2):244–56 doi 10.1016/j.ccr.2010.12.021. [PubMed: 21316603]
16. Stewart CA, Gay CM, Xi Y, Sivajothi S, Sivakamasundari V, Fujimoto J, et al. Single-cell analyses reveal increased intratumoral heterogeneity after the onset of therapy resistance in small-cell lung cancer. Nature Cancer 2020;1(4):423–36 doi 10.1038/s43018-019-0020-z. [PubMed: 33521652]
17. Oliveira CC, van Hall T. Alternative Antigen Processing for MHC Class I: Multiple Roads Lead to Rome. Front Immunol 2015;6:298 doi 10.3389/fimmu.2015.00298. [PubMed: 26097483]
18. de Charette M, Marabelle A, Houot R. Turning tumour cells into antigen presenting cells: The next step to improve cancer immunotherapy? Eur J Cancer 2016;68:134–47 doi 10.1016/j.ejca.2016.09.010. [PubMed: 27755997]
19. Leone P, Shin EC, Perosa F, Vacca A, Dammacco F, Racanelli V. MHC class I antigen processing and presenting machinery: organization, function, and defects in tumor cells. J Natl Cancer Inst 2013;105(16):1172–87 doi 10.1093/jnci/djt184. [PubMed: 23852952]
20. Restifo NP, Esquivel F, Kawakami Y, Yewdell JW, Mule JJ, Rosenberg SA, et al. Identification of human cancers deficient in antigen processing. J Exp Med 1993;177(2):265–72 doi 10.1084/jem.177.2.265. [PubMed: 8426105]
21. Doyle A, Martin WJ, Funa K, Gazdar A, Carney D, Martin SE, et al. Markedly decreased expression of class I histocompatibility antigens, protein, and mRNA in human small-cell lung cancer. J Exp Med 1985;161(5):1135–51 doi 10.1084/jem.161.5.1135. [PubMed: 2580935]
22. Funa K, Gazdar AF, Minna JD, Linnoila RI. Paucity of beta 2-microglobulin expression on small cell lung cancer, bronchial carcinoids and certain other neuroendocrine tumors. Lab Invest 1986;55(2):186–93. [PubMed: 3525983]
23. Burr ML, Sparbier CE, Chan KL, Chan YC, Kersbergen A, Lam EYN, et al. An Evolutionarily Conserved Function of Polycomb Silences the MHC Class I Antigen Presentation Pathway and Enables Immune Evasion in Cancer. Cancer Cell 2019;36(4):385–401 e8 doi 10.1016/j.ccell.2019.08.008. [PubMed: 31564637]
24. Williamson SC, Metcalf RL, Trapani F, Mohan S, Antonello J, Abbott B, et al. Vasculogenic mimicry in small cell lung cancer. Nat Commun 2016;7:13322 doi 10.1038/ncomms13322. [PubMed: 27827359]
25. Schultheis AM, Scheel AH, Ozretic L, George J, Thomas RK, Hagemann T, et al. PD-L1 expression in small cell neuroendocrine carcinomas. Eur J Cancer 2015;51(3):421–6 doi 10.1016/j.ejca.2014.12.006. [PubMed: 25582496]
26. Canadas I, Rojo F, Taus A, Arpi O, Arumi-Uria M, Pijuan L, et al. Targeting epithelial-to-mesenchymal transition with Met inhibitors reverts chemoresistance in small cell lung cancer. Clin Cancer Res 2014;20(4):938–50 doi 10.1158/1078-0432.CCR-13-1330. [PubMed: 24284055]
27. Balanis NG, Sheu KM, Esedebe FN, Patel SJ, Smith BA, Park JW, et al. Pan-cancer Convergence to a Small-Cell Neuroendocrine Phenotype that Shares Susceptibilities with Hematological Malignancies. Cancer Cell 2019;36(1):17–34 e7 doi 10.1016/j.ccell.2019.06.005. [PubMed: 31287989]
28. Gardner EE, Lok BH, Schneeberger VE, Desmeules P, Miles LA, Arnold PK, et al. Chemosensitive Relapse in Small Cell Lung Cancer Proceeds through an EZH2-SLFN11 Axis. Cancer Cell 2017;31(2):286–99 doi 10.1016/j.ccell.2017.01.006. [PubMed: 28196596]

29. Poirier JT, Gardner EE, Connis N, Moreira AL, de Stanchina E, Hann CL, et al. DNA methylation in small cell lung cancer defines distinct disease subtypes and correlates with high expression of EZH2. Oncogene 2015;34(48):5869–78 doi 10.1038/onc.2015.38. [PubMed: 25746006]
30. Oser MG, Sabet AH, Gao W, Chakraborty AA, Schinzel AC, Jennings RB, et al. The KDM5A/RBP2 histone demethylase represses NOTCH signaling to sustain neuroendocrine differentiation and promote small cell lung cancer tumorigenesis. Genes Dev 2019;33(23–24):1718–38 doi 10.1101/gad.328336.119. [PubMed: 31727771]
31. Zhang H, Christensen CL, Dries R, Oser MG, Deng J, Diskin B, et al. CDK7 Inhibition Potentiates Genome Instability Triggering Anti-tumor Immunity in Small Cell Lung Cancer. Cancer Cell 2020;37(1):37–54 e9 doi 10.1016/j.ccell.2019.11.003. [PubMed: 31883968]
32. Lizotte PH, Hong RL, Luster TA, Cavanaugh ME, Taus LJ, Wang S, et al. A High-Throughput Immune-Oncology Screen Identifies EGFR Inhibitors as Potent Enhancers of Antigen-Specific Cytotoxic T-lymphocyte Tumor Cell Killing. Cancer Immunol Res 2018;6(12):1511–23 doi 10.1158/2326-6066.CIR-18-0193. [PubMed: 30242021]
33. Poczobutt JM, De S, Yadav VK, Nguyen TT, Li H, Sippel TR, et al. Expression Profiling of Macrophages Reveals Multiple Populations with Distinct Biological Roles in an Immunocompetent Orthotopic Model of Lung Cancer. J Immunol 2016;196(6):2847–59 doi 10.4049/jimmunol.1502364. [PubMed: 26873985]
34. Goswami S, Apostolou I, Zhang J, Skepner J, Anandhan S, Zhang X, et al. Modulation of EZH2 expression in T cells improves efficacy of anti-CTLA-4 therapy. J Clin Invest 2018;128(9):3813–8 doi 10.1172/JCI99760. [PubMed: 29905573]
35. Zhou L, Mudianto T, Ma X, Riley R, Uppaluri R. Targeting EZH2 Enhances Antigen Presentation, Antitumor Immunity, and Circumvents Anti-PD-1 Resistance in Head and Neck Cancer. Clin Cancer Res 2020;26(1):290–300 doi 10.1158/1078-0432.CCR-19-1351. [PubMed: 31562203]
36. Gay CM, Stewart CA, Park EM, Diao L, Groves SM, Heeke S, et al. Patterns of transcription factor programs and immune pathway activation define four major subtypes of SCLC with distinct therapeutic vulnerabilities. Cancer Cell 2021 doi 10.1016/j.ccell.2020.12.014.
37. Ott PA, Elez E, Hiret S, Kim DW, Morosky A, Saraf S, et al. Pembrolizumab in Patients With Extensive-Stage Small-Cell Lung Cancer: Results From the Phase Ib KEYNOTE-028 Study. J Clin Oncol 2017;35(34):3823–9 doi 10.1200/JCO.2017.72.5069. [PubMed: 28813164]
38. Antonia SJ, Lopez-Martin JA, Bendell J, Ott PA, Taylor M, Eder JP, et al. Nivolumab alone and nivolumab plus ipilimumab in recurrent small-cell lung cancer (CheckMate 032): a multicentre, open-label, phase 1/2 trial. Lancet Oncol 2016;17(7):883–95 doi 10.1016/S1470-2045(16)30098-5. [PubMed: 27269741]
39. Hellmann MD, Callahan MK, Awad MM, Calvo E, Ascierto PA, Atmaca A, et al. Tumor Mutational Burden and Efficacy of Nivolumab Monotherapy and in Combination with Ipilimumab in Small-Cell Lung Cancer. Cancer Cell 2019;35(2):329 doi 10.1016/j.ccell.2019.01.011. [PubMed: 30753829]
40. Konieczkowski DJ, Johannessen CM, Abudayyeh O, Kim JW, Cooper ZA, Piris A, et al. A melanoma cell state distinction influences sensitivity to MAPK pathway inhibitors. Cancer Discov 2014;4(7):816–27 doi 10.1158/2159-8290.CD-13-0424. [PubMed: 24771846]
41. Kitajima S, Ivanova E, Guo S, Yoshida R, Campisi M, Sundararaman SK, et al. Suppression of STING Associated with LKB1 Loss in KRAS-Driven Lung Cancer. Cancer Discov 2019;9(1):34–45 doi 10.1158/2159-8290.CD-18-0689. [PubMed: 30297358]
42. Sen T, Rodriguez BL, Chen L, Corte CMD, Morikawa N, Fujimoto J, et al. Targeting DNA Damage Response Promotes Antitumor Immunity through STING-Mediated T-cell Activation in Small Cell Lung Cancer. Cancer Discov 2019;9(5):646–61 doi 10.1158/2159-8290.CD-18-1020. [PubMed: 30777870]
43. Dunn J, Rao S. Epigenetics and immunotherapy: The current state of play. Mol Immunol 2017;87:227–39 doi 10.1016/j.molimm.2017.04.012. [PubMed: 28511092]
44. Dunn GP, Old LJ, Schreiber RD. The immunobiology of cancer immunosurveillance and immunoediting. Immunity 2004;21(2):137–48 doi 10.1016/j.immuni.2004.07.017. [PubMed: 15308095]

45. Sholl LM, Do K, Shivdasani P, Cerami E, Dubuc AM, Kuo FC, et al. Institutional implementation of clinical tumor profiling on an unselected cancer population. JCI Insight 2016;1(19):e87062 doi 10.1172/jci.insight.87062. [PubMed: 27882345]
46. Wickstrom SL, Lovgren T, Volkmar M, Reinhold B, Duke-Cohan JS, Hartmann L, et al. Cancer Neoepitopes for Immunotherapy: Discordance Between Tumor-Infiltrating T Cell Reactivity and Tumor MHC Peptidome Display. Front Immunol 2019;10:2766 doi 10.3389/fimmu.2019.02766. [PubMed: 31921104]
47. Cornwell M, Vangala M, Taing L, Herbert Z, Koster J, Li B, et al. VIPER: Visualization Pipeline for RNA-seq, a Snakemake workflow for efficient and complete RNA-seq analysis. BMC Bioinformatics 2018;19(1):135 doi 10.1186/s12859-018-2139-9. [PubMed: 29649993]
48. Anders S, Huber W. Differential expression analysis for sequence count data. Genome Biol 2010;11(10):R106 doi 10.1186/gb-2010-11-10-r106. [PubMed: 20979621]
49. Yu G, Wang LG, Han Y, He QY. clusterProfiler: an R package for comparing biological themes among gene clusters. OMICS 2012;16(5):284–7 doi 10.1089/omi.2011.0118. [PubMed: 22455463]
50. Subramanian A, Tamayo P, Mootha VK, Mukherjee S, Ebert BL, Gillette MA, et al. Gene set enrichment analysis: a knowledge-based approach for interpreting genome-wide expression profiles. Proc Natl Acad Sci U S A 2005;102(43):15545–50 doi 10.1073/pnas.0506580102. [PubMed: 16199517]
51. Sato T, Yoo S, Kong R, Sinha A, Chandramani-Shivalingappa P, Patel A, et al. Epigenomic Profiling Discovers Trans-lineage SOX2 Partnerships Driving Tumor Heterogeneity in Lung Squamous Cell Carcinoma. Cancer Res 2019;79(24):6084–100 doi 10.1158/0008-5472.CAN-19-2132. [PubMed: 31551362]
52. Zhang Y, Liu T, Meyer CA, Eeckhoute J, Johnson DS, Bernstein BE, et al. Model-based analysis of ChIP-Seq (MACS). Genome Biol 2008;9(9):R137 doi 10.1186/gb-2008-9-9-r137. [PubMed: 18798982]
53. Robinson JT, Thorvaldsdottir H, Winckler W, Guttman M, Lander ES, Getz G, et al. Integrative genomics viewer. Nat Biotechnol 2011;29(1):24–6 doi 10.1038/nbt.1754. [PubMed: 21221095]
54. Doench JG, Fusi N, Sullender M, Hegde M, Vaimberg EW, Donovan KF, et al. Optimized sgRNA design to maximize activity and minimize off-target effects of CRISPR-Cas9. Nat Biotechnol 2016;34(2):184–91 doi 10.1038/nbt.3437. [PubMed: 26780180]
55. Sanjana NE, Shalem O, Zhang F. Improved vectors and genome-wide libraries for CRISPR screening. Nat Methods 2014;11(8):783–4 doi 10.1038/nmeth.3047. [PubMed: 25075903]
56. Shalem O, Sanjana NE, Hartenian E, Shi X, Scott DA, Mikkelson T, et al. Genome-scale CRISPR-Cas9 knockout screening in human cells. Science 2014;343(6166):84–7 doi 10.1126/science.1247005. [PubMed: 24336571]
57. Butler A, Hoffman P, Smibert P, Papalexi E, Satija R. Integrating single-cell transcriptomic data across different conditions, technologies, and species. Nat Biotechnol 2018;36(5):411–20 doi 10.1038/nbt.4096. [PubMed: 29608179]
58. Aibar S, Gonzalez-Blas CB, Moerman T, Huynh-Thu VA, Imrichova H, Hulselmans G, et al. SCENIC: single-cell regulatory network inference and clustering. Nat Methods 2017;14(11):1083–6 doi 10.1038/nmeth.4463. [PubMed: 28991892]
59. Han X, Wang R, Zhou Y, Fei L, Sun H, Lai S, et al. Mapping the Mouse Cell Atlas by Microwell-Seq. Cell 2018;173(5):1307 doi 10.1016/j.cell.2018.05.012. [PubMed: 29775597]
60. Holst J, Szymczak-Workman AL, Vignali KM, Burton AR, Workman CJ, Vignali DA. Generation of T-cell receptor retrogenic mice. Nat Protoc 2006;1(1):406–17 doi 10.1038/nprot.2006.61. [PubMed: 17406263]
61. Brazin KN, Mallis RJ, Boeszoermenyi A, Feng Y, Yoshizawa A, Reche PA, et al. The T Cell Antigen Receptor alpha Transmembrane Domain Coordinates Triggering through Regulation of Bilayer Immersion and CD3 Subunit Associations. Immunity 2018;49(5):829–41 e6 doi 10.1016/j.immuni.2018.09.007. [PubMed: 30389415]
62. Aref AR, Campisi M, Ivanova E, Portell A, Larios D, Piel BP, et al. 3D microfluidic ex vivo culture of organotypic tumor spheroids to model immune checkpoint blockade. Lab Chip 2018;18(20):3129–43 doi 10.1039/c8lc00322j. [PubMed: 30183789]

63. Shin Y, Han S, Jeon JS, Yamamoto K, Zervantonakis IK, Sudo R, et al. Microfluidic assay for simultaneous culture of multiple cell types on surfaces or within hydrogels. Nat Protoc 2012;7(7):1247–59 doi 10.1038/nprot.2012.051. [PubMed: 22678430]

Significance

SCLC is poorly immunogenic, displaying modest ICB responsiveness with rare durable activity. In profiling its plasticity, we uncover intrinsically immunogenic MHC I^{hi} subpopulations of non-neuroendocrine SCLC associated with durable ICB benefit. We also find that combined EZH2 inhibition and STING agonism uncovers this cell state, priming cells for immune rejection.

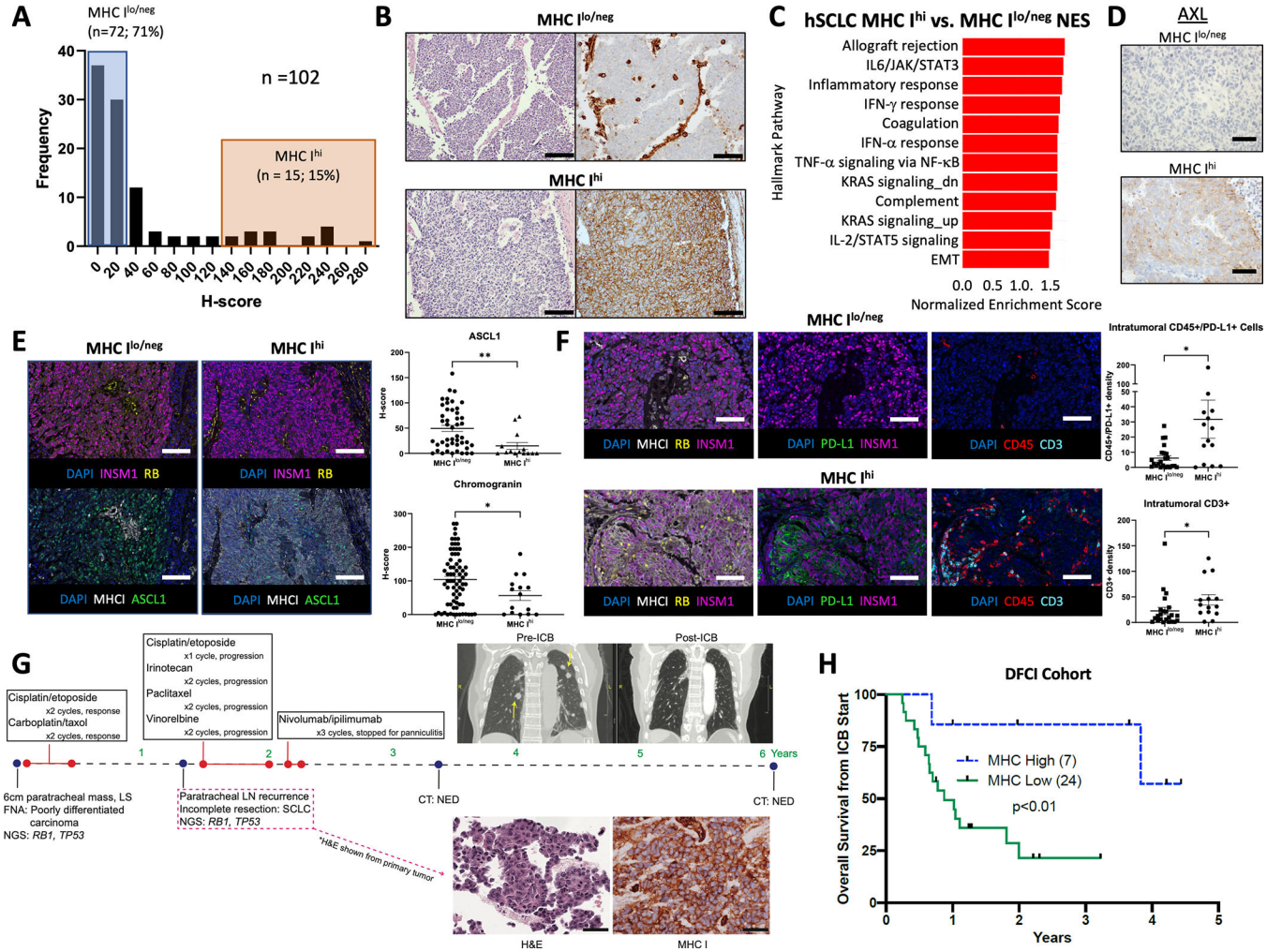

Figure 1.

MHC Class I expression is increased in patient SCLC with non-neuroendocrine features, which is enriched in exceptional responders to immune checkpoint blockade. **A,** Frequency distribution of MHC Class I (MHC I) expression expressed as H-score in patient SCLC tumors (n=102). **B,** Representative micrographs of H&E and MHC I IHC in (*top*) MHC I low/negative (MHC $I^{lo/neg}$) and (*bottom*) MHC I uniformly high (MHC I^{hi}) patient SCLC tumors. Scale bar indicates 100 μm. **C,** Gene Set Enrichment Analysis (GSEA) based on the RNAseq expression fold-change values of MHC I^{hi} vs. MHC $I^{lo/neg}$ patient SCLC tumors. Bar plot represents normalized enrichment scores (NES) for the top upregulated Hallmark gene. **D,** Representative micrographs of AXL IHC in (*top*) MHC $I^{lo/neg}$ and (*bottom*) MHC I^{hi} patient SCLC tumors. Scale bar indicates 50 μm. **E**, (*left*) Representative multiplexed immunofluorescence images of MHC $I^{lo/neg}$ and MHC I^{hi} patient SCLC tumors displaying expression of indicated proteins. (*right*) Quantification of ASCL1 and chromogranin expression by H-score in MHC I^{hi} and MHC $I^{lo/neg}$ patient SCLC tumors. Error bars indicate mean ± s.e.m. **F**, (*left*) Representative multiplexed immunofluorescence images of MHC $I^{lo/neg}$ and MHC I^{hi} patient SCLC tumors displaying intratumoral infiltration of immune cells marked by expression of indicated proteins. (*right*) Digital image quantification of

indicated immune cell subsets in MHC I^{hi} and MHC $I^{lo/neg}$ patient SCLC tumors intratumorally (tumor) or at the tumor/stroma interface (tumor/stroma). **G,** Immunophenotypic characterization of tumors and associated clinical courses of a SCLC patient with an exceptional response to immune checkpoint blockade (ICB) therapy. Clinical stage at diagnosis is indicated as limited stage (LS). Next-generation sequencing (NGS) results indicating loss-of-function variants or deletions of key SCLC tumor suppressor genes are listed. NED = no evidence of disease. **H,** Kaplan-Meier curves displaying overall survival of SCLC patients from initiation of immune checkpoint blockade (ICB), stratified by tumor MHC I IHC expression. *P* values were calculated using a two-tailed Mann-Whitney test (**E, F**), or log-rank test (**H**). *, $P < 0.05$; **, $P < 0.01$.

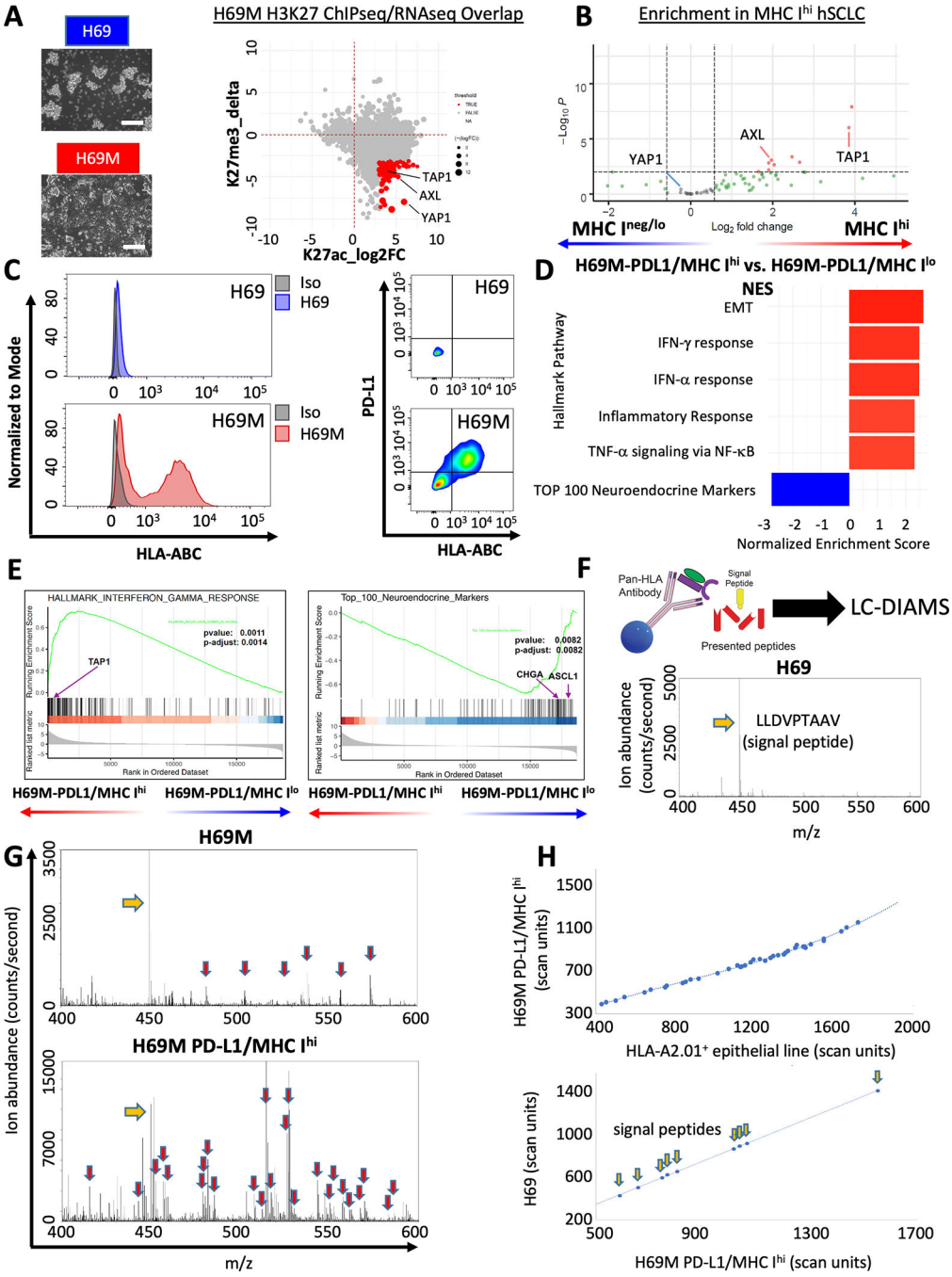

Figure 2.

Modeling plastic SCLC cell states *in vitro* reveals immunologically distinct SCLC subpopulations. **A,** (*left*) Phase contrast images of suspension H69 and adherent H69M SCLC cell lines. (*right*) Bivariate plot of normalized H3K27Me3 and H3K27Ac signal intensity in H69M cells at all gene loci derived from RNAseq data set. Scale bars indicate 100 μm. **B,** Volcano plot for genes showing significantly increased H3K27Ac and decreased H3K27Me3 indicated in red in (**A**) in MHC I^{hi} vs. MHC I$^{lo/neg}$ patient SCLC tumors. **C,** Flow cytometric analysis of HLA-ABC and PD-L1 expression on H69 and H69M

(representative of n=3 independent experiments). **D, E,** Gene Set Enrichment Analysis (GSEA) based on the expression fold-change values in H69M PD-L1/MHC I^{hi} vs. H69M PD-L1/MHC I^{lo} samples. Bar plot (**D**) represents normalized enrichment scores (NES) for the top Hallmark gene sets and neuroendocrine gene set (27), and GSEA plots for IFN-γ response and neuroendocrine (27) gene sets are shown in (**E**). Arrows mark rank positions of indicated genes. **F,** (*top*) Schematic of pan-HLA I immunopeptidome analysis. (*bottom*) Mass spectrum of HLA I-complexed peptides recovered from H69 cells at the point in the chromatogram where the signal peptide LLDVPTAAV elutes (molecular ion at m/z 449.76 marked by yellow arrow). Minor co-eluting ions are chemical background. **G,** Mass spectrum of HLA I-complexed peptides recovered from H69M and H69M PD-L1/MHC I^{hi} cells shown at the elution position of the LLDVPTAAV signal peptide (yellow arrow). Red arrows indicate positions of doubly charged ions corresponding to distinct co-eluting HLA-I complexed endogenously processed (TAP-dependent) peptides. **H,** Paired elution positions of shared peptides detected in different samples forms an elution line, a mark of correct identification. Elution positions of a reference set of HLA-A2.01-restricted peptides in H69M PD-L1/MHC I^{hi} cells as a function of the elution positions of this set detected in an HLA-A2.01+ epithelial line and H69M PD-L1/MHC I^{hi} cells (*top*) vs. H69 cells (*bottom*). Yellow arrows indicate paired elution positions of known signal peptides. Adjusted *P* values were calculated using the al Benjamini & Hochberg (BH) method (**E)**.

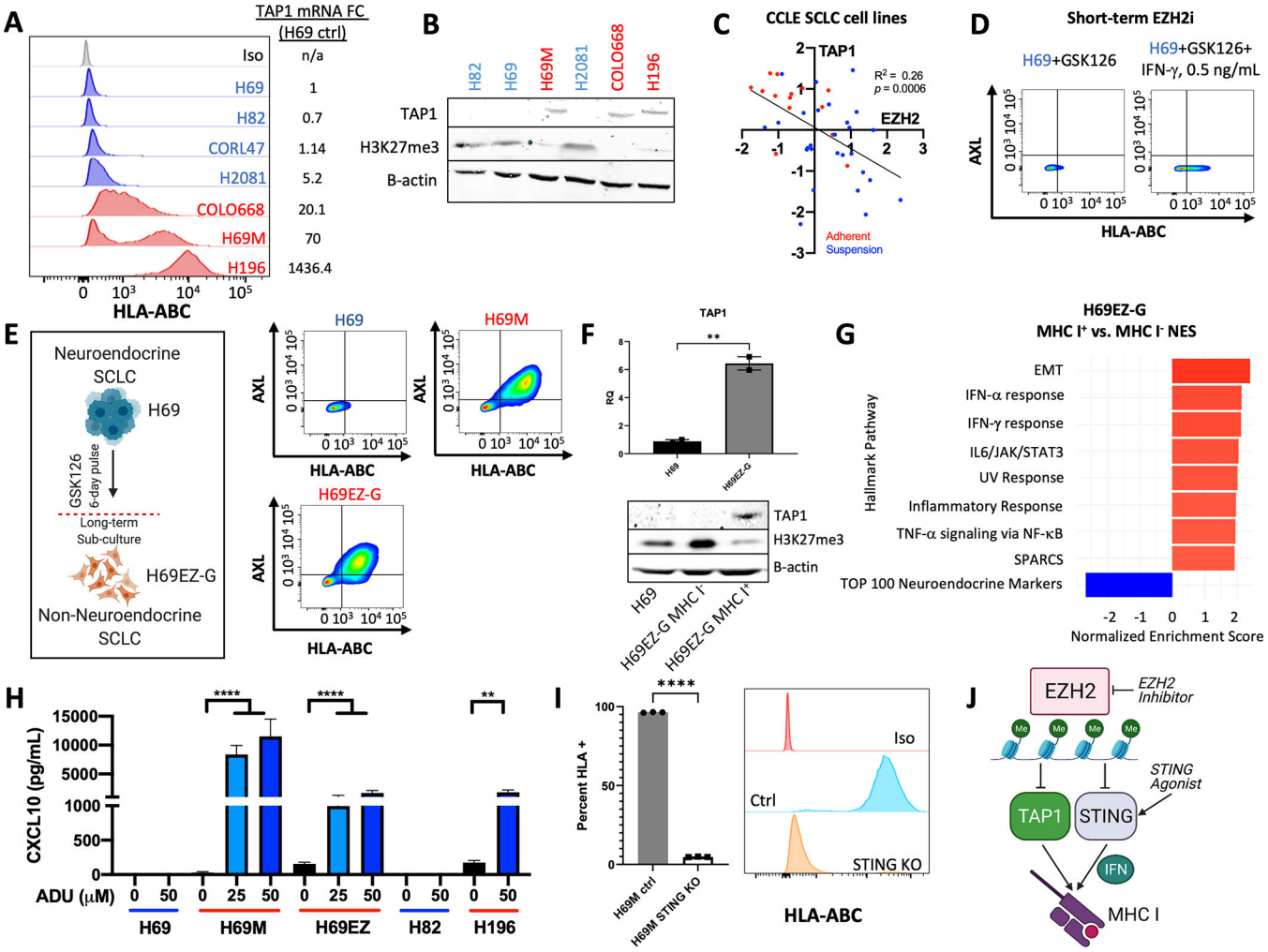

Figure 3.

EZH2 inhibition promotes the non-neuroendocrine antigenic SCLC state. **A,** (*left*) Flow cytometric analysis of HLA-ABC expression on the indicated suspension, neuroendocrine (blue) and adherent, non-neuroendocrine (red) SCLC cell lines (representative of n=2 independent experiments) and (*right*) associated qRT-PCR relative quantification (RQ) values of TAP1 expression normalized to H69 cells. **B,** Immunoblot of TAP1, H3K27Me3, and B-actin levels in indicated suspension, neuroendocrine (blue) and adherent, non-neuroendocrine (red) SCLC cell lines. **C,** Bivariate plot of Log2 fold change in mRNA expression (normalized by robust multi-array analysis [RMA]) of *TAP1* and *EZH2* in suspension and adherent SCLC cell lines from the CCLE. **D,** Flow cytometric analysis of HLA-ABC and AXL expression in H69 cells treated with GSK126 (5 μM) +/− 24 h IFN-γ. **E**, (*left*) Schematic of non-neuroendocrine cell state change induced by transient EZH2 inhibition in neuroendocrine SCLC via 6 d GSK126 (5 μM) pulse followed by long term sub-culture without drug. Schematic created with BioRender.com. (*right*) Flow cytometric analysis of HLA-ABC and AXL expression in indicated stable cell lines at basal conditions (representative of n=2 independent experiments). **F,** (*top*) qRT-PCR of *TAP1* in H69EZ-G normalized to H69 cells (RQ), representative of n=2 independent experiments. Error bars are

mean ± s.e.m. of n=2 biological replicates. (*bottom*) Immunoblot of TAP1, H3K27Me3, and B-actin levels in H69 cells and HLA-ABC-positive (+) or negative (–) fractions sorted from H69EZ-G cells. **G,** Gene Set Enrichment Analysis (GSEA) based on the expression fold-change values of MHC I^{hi} vs. MHC $I^{lo/neg}$ patient SCLC tumors. Bar plot represents normalized enrichment scores (NES) for the top Hallmark gene sets, SPARCS gene set (13), neuroendocrine gene set (27). **H,** CXCL10 secretion by indicated suspension, neuroendocrine (blue) and adherent, non-neuroendocrine (red) SCLC cell lines upon 24 h treatment with indicated concentrations of ADU-S100. Error bars are mean ± s.e.m of n=3 biological replicates. **I,** (*left*) Histogram of percent HLA+ cells in indicated H69M cell lines, as measured by flow cytometry. Error bars are mean ± s.e.m of n=3 biological replicates. (*right*) Representative flow cytometric analysis of HLA-ABC expression in indicated cell lines. **J,** Schematic of postulated de-repression of MHC Class I expression in non-neuroendocrine SCLC cells, and proposed therapeutic activation of this pathway in neuroendocrine SCLC cells with combined EZH2 inhibition and STING agonism. Schematic created with BioRender.com. *P* values were calculated using an unpaired two-tailed Student's t test (**F, I**) or Bonferroni corrected pairwise comparisons after an ANOVA global test (**H**). **, $P < 0.01$; ****, $P < 0.0001$; n.s., not significant. R^2 and associated *p* value (**C**) represents Pearson correlation coefficient.

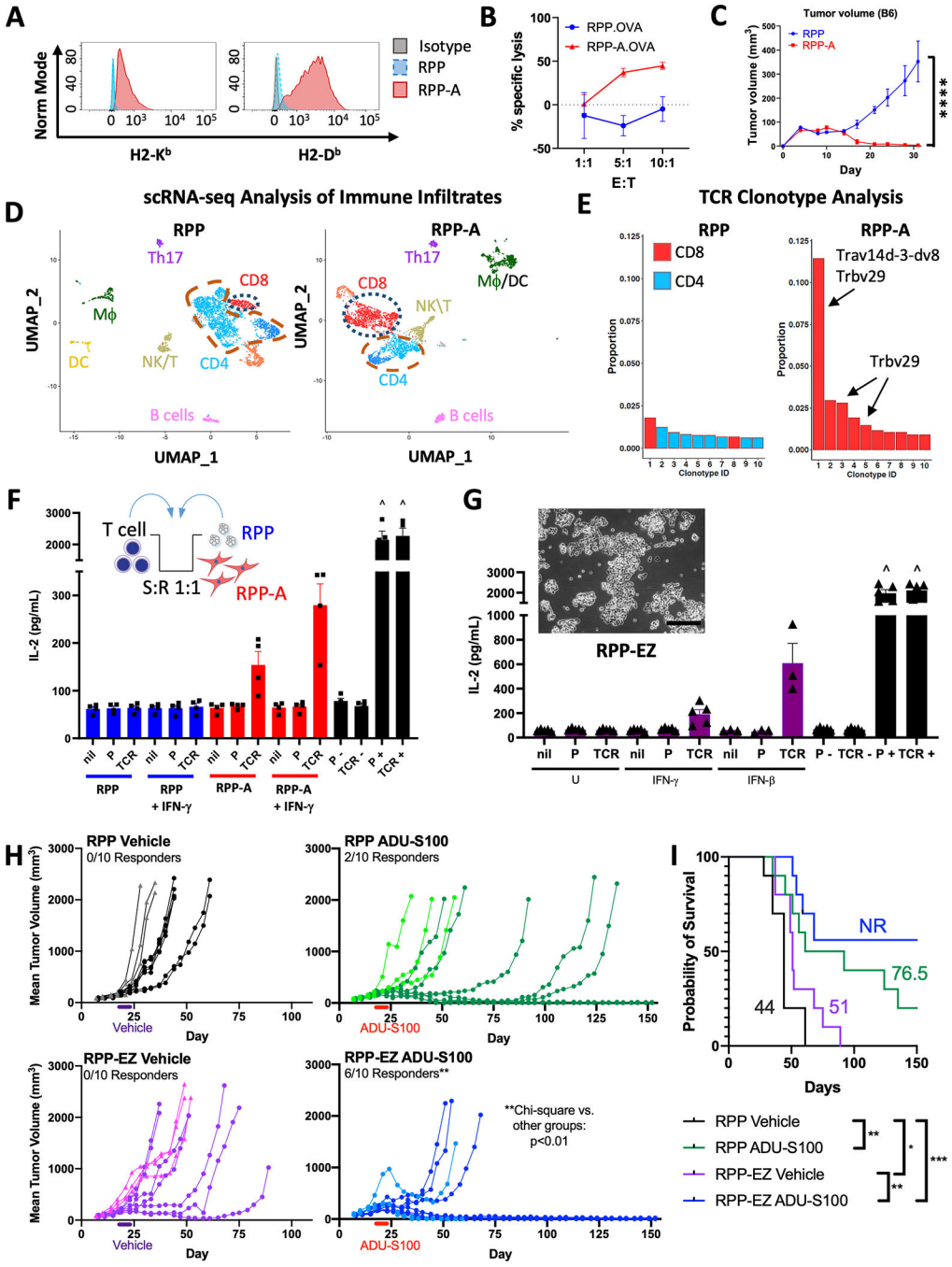

Figure 4.

Non-neuroendocrine SCLC cells are immunogenic *in vitro* and *in vivo*. **A,** Flow cytometric analysis of MHC Class I allele (H2-K^b and H2-D^b) expression on indicated SCLC cell lines (representative of n=5 independent experiments). **B,** Specific lysis of RPP.OVA or RPP-A.OVA cells after 48 h co-culture with activated CD8+ T cells from OT-I mice at indicated effector:target (E:T) ratios (representative of n=2 independent experiments). Each data point represents mean ± s.e.m. of triplicate wells. **C,** Tumor volume measurements of RPP and RPP-A cells after s.c. inoculation into syngeneic C57/BL6 mice. Each data point represents

mean ± s.e.m. tumor volumes (n=5 in RPP group and n=5 in RPP-A group). **D,** UMAP plots displaying unsupervised clustering of single-cell RNA sequencing data for CD45+ cells from RPP and RPP-A tumors formed from (**C**) at day 14. Labels indicate cell assignment based on comparison of cluster gene expression signatures from Han et al.(59) CD8 and CD4 T cells are indicated in each tumor. **E,** Frequency of top 10 TCR clonotypes in RPP and RPP-A tumors. The α/β chains of the immunodominant TCR in RPP-A tumors, as well as the β chain shared among clonotypes, are indicated by arrows. **F,** (*top*) Schematic of tumor cell-T cell co-culture, performed at a stimulator:responder (S:R) ratio of 1:1. (*bottom*) IL-2 secretion from 72 h co-cultures of RPP (blue bars) or RPP-A (red bars) cells +/− 24 h IFN-γ (100 ng/mL) stimulation and no (nil), parental untransduced BW5147.3 (P), or Trav14D-3-DV8; Trbv29 transgenic BW5147.3 (TCR) T cells. Black bars represent P or TCR T cells alone without (–) or with (+) PMA (50 nM) and Ionomycin (1 μg/mL). ^ = above assay threshold of detection. Error bars are mean ± s.e.m of n=4 independent experiments. **G**, (*top*) Phase contrast image of RPP-EZ SCLC cell line. Scale bar indicates 100 μm. (*bottom*) IL-2 secretion from 72 h co-cultures of RPP-EZ cells +/− 24 h IFN-γ (100 ng/mL) or IFN-β (100 ng/mL) stimulation and no (nil), parental untransduced BW5147.3 (P), or Trav14D-3-DV8; Trbv29 transgenic BW5147.3 (TCR) T cells. Black bars represent P or TCR T cells alone without (–) or with (+) PMA (50 nM) and Ionomycin (1 μg/mL). ^ = above assay threshold of detection. Error bars are mean ± s.e.m of n=3–5 independent experiments. **H,** Tumor volume measurements of RPP-EZ or RPP cells after subcutaneous inoculation into syngeneic C57/BL6 mice followed by intratumoral vehicle or ADU-S100 treatments (first treatment, 50 μg; second treatment, 35 μg) on indicated days (day 19/23 for Cohort 1 [n=7, darker shade shade with squares]; day 21/24 for Cohort 2 [n=3 mice per group; lighter shade with triangles]). The number of responders, defined as minimal residual tumors that are not resolved for the duration of the study and/or no measurable tumors for more than 7 doubling times, is indicated for each group. **I,** Kaplan-Meier curves displaying survival of mice from (**H**). *P* values were calculated using a log-rank test (**C, I**) and chi-square test (**H**). *, $P < 0.05$; **, $P < 0.01$; ***, $P < 0.001$; ****, $P < 0.0001$.